Measurement and Prediction of Radiative Non-equilibrium for Air Shocks Between 7-9 km/s

Brett A. Cruden,[1] Aaron M. Brandis[2]
AMA, Inc. at NASA Ames Research Center, Moffett Field, CA, 94035

The present paper describes a recent characterization of thermochemical non-equilibrium for shock speeds between 7 and 9 km/s in the NASA Ames Electric Arc Shock Tube (EAST) Facility. Data are spectrally resolved from 190-1450 nm and spatially resolved behind the shock front. The data are analyzed in terms of a spectral non-equilibirum metric, defined as the average radiance within ±2 cm of the peak. Simulations with DPLR/NEQAIR using different rate chemistries show these conditions to be poorly replicated. The sources of discrepancy are examined, leading to an update to the NEQAIR non-Boltzmann model and DPLR rate chemistry. New parameters for the rate chemistry and non-Boltzmann modeling are reported.

I. Introduction

In recent years, extensive campaigns have been conducted to measure shock-layer radiation at velocities from 9-15 km/s.[1] However, there are little recent data characterizing the radiation below this velocity range. Although the radiative heat flux magnitudes in this velocity region are relatively small, it can contribute a significant amount to heat load. Using lunar return as an example, around 10% of the radiative heat load may originate from velocities less than 9 km/s. For entries from low earth orbit, this velocity range comprises the entirety of radiative heating. In contrast to high velocity entries, a significant fraction of radiation at low velocity in air originates from molecular species such as NO, N_2 and N_2^+. This therefore represents a different regime for radiation and exercises portions of the model that are not tested at higher velocity conditions.

Therefore, a test series has been undertaken in the EAST facility to characterize radiation in this velocity range, the results of which are reported here. Experiments were conducted between 7-9 km/s, at six different freestream pressures from 0.01-0.70 Torr. The experiment is described in section II. Simulations of these experiments were carried out with the DPLR and NEQAIR codes with 12 different modelling options, described in section III. Since the amount of data (measured and simulated) is voluminous, only a subset of results is presented to preserve clarity and to provide general conclusions about the state of predictive modelling in section IV. The results have prompted an examination of the modeling parameters in DPLR/NEQAIR which is conducted in section V. Finally, the comparison of the revised model to the experimental data is given in section VI. This work provides an updated approach to simulating air radiation at low velocities. While some areas for further development remain, the model should be tested at a wider range of test conditions to confirm its broader applicability.

II. Experiment

The EAST facility has been described in detail in previous work and so is only briefly summarized here [2]. A 1.2 MJ, 40 kV capacitor bank drives one of two shock tubes. The first is a 60.33 cm inner diameter stainless steel tube, intended for testing at low density, and the second is a 10.16 cm aluminum tube which has been extensively utilized in high velocity testing in recent years. The observation section is located 21.4 m downstream of the diaphragm in the 60 cm tube and 7.9 m downstream in the 10 cm tube. The radiance is imaged axially onto spectrometers, producing spectrally and spatially resolved radiance data in each test. On the 60 cm tube, two spectrometers are simultaneously in use, while four spectrometers are used simultaneously on the 10 cm tube. Between these spectrometers, radiance is measured from 190-540 nm and/or 480-1450 nm with each test.

Tests in the 60 cm tube were conducted with initial pressures of 0.01, 0.05 and 0.14 Torr, while the 10 cm tube was employed at pressures of 0.14, 0.30, 0.50 and 0.70 Torr. The velocities spanned 6.8-9.2 km/s, with higher

[1] Sr. Research Scientist, Aerothermodynamics Branch. Associate Fellow AIAA. Contact: brett.a.cruden@nasa.gov
[2] Sr. Research Scientist, Aerothermodynamics Branch. Senior Member AIAA.

velocities generally being tested at lower pressures. A total of 51 tests were conducted, 33 of which were performed in the 60 cm tube. Of these tests, 44 were deemed to have acceptable data quality. For each of the six pressures examined, one representative test is selected for further analysis. To provide analysis at all wavelengths and on both tubes requires 10 shots to be analyzed. The conditions of these shots are shown in Table 1.

Table 1. Shot conditions presented in this work

Shot No	Velocity (km/s)	Pressure (torr)	Range (nm)	Tube Diameter (cm)
15	8.18	0.01	190-500	60.33
32	8.57	0.01	500-1450	60.33
8	8.62	0.05	190-500	60.33
24	8.87	0.05	500-1450	60.33
20	8.29	0.14	190-500	60.33
22	8.36	0.14	500-1450	60.33
38	8.33	0.14	190-1450	10.16
42	8.09	0.3	190-1450	10.16
46	7.71	0.5	190-1450	10.16
50	7.34	0.7	190-1450	10.16

III. Simulation

In order to simulate these results, it is assumed that the shock tube measurements show similarity to the stagnation line over a blunt body. A 3-m diameter sphere is simulated using DPLR v4.04.0.[3] The stagnation line is then passed to NEQAIR15[4], where radiance is calculated perpendicular to the line-of-sight direction (i.e. "shock tube" mode) to create a radiation profile along the tube axis. In order to investigate the performance of existing tools and models, this was undertaken using different available modeling options. The options are summarized in Table 2.

Table 2. Thermophysical modeling options employed in the present work

Modeling Option	Models
Electron(ic) Energy	(a) $T_e=T_t$, (b) $T_e=T_v$
Chemical Kinetics	(a) Park90 [5], (b) Park93 [6], (c) Johnston14 [7]
Impact Excitation	(a) Park [5], (b) Huo [8]

The first option involves how electron and electronic energy are accounted for within the context of the two-temperature model. Traditionally, DPLR has assumed energy stored in these modes to be determined by a combined translational-rotational-electronic temperature ($T=T_t=T_r=T_e$), with a separate temperature, T_v, used to describe vibrational energy. In contrast, other codes such as LAURA[9] have assumed the vibrational and electronic modes to be lumped. The traditional DPLR approach poses a difficulty for radiation solutions as the large translational temperatures obtained in thermal non-equilibrium result in excessive radiation from electronic states. The solution had been to set the electronic temperature to the vibrational temperature when the DPLR stagnation line was parsed to the radiation code, even though it was inconsistent with the way the CFD solution was run. DPLR v4.04.0 now provides an option to simulate the energy partition with a lumped vibrational-electronic temperature, thus removing the need for the above workaround.

The second option is the chemical kinetic model used to produce the chemical non-equilibrium solution. Traditionally, the rates published in Park's 1990 text have been employed by NASA flight projects.[5] In 1993, Park published an update to these rates which is also run in this work.[6] The third chemistry model uses the rates employed by Johnston in 2014[7], which are the rates currently used with the LAURA CFD code. These rates are largely based on the work of Park, though some have been modified based on more recent studies.[10-14] A summary of the differences in the three rate models is given in Table 3. From the table it is seen that six rates were altered from Park90 to Park93 while Johnston14 employs ten different rates from Park90. An additional variable that was not adjustable here is the controlling temperature for different reactions. It has long been standard practice in DPLR to use $\sqrt{TT_v}$ as the controlling temperature for dissociation reactions and T as the controlling temperature for other reactions.

The final variation examined within the NEQAIR code is the electron impact rates which determine the state populations in non-equilibrium (i.e. non-Boltzmann distributions). The standard release of the NEQAIR code uses rates from the work of Park [5]. More recently, new rates for N, O and C have been calculated and compiled by Huo [8]. These rates are similar to those utilized by the HARA code.

Table 3. Summary of reaction rate sources by kinetic rate model

Reaction	Park 90	Park 93[a]	Johnston 2014[b]
$N_2 + M \leftrightarrow 2N + M$	[5]	[5]	[5]
$O_2 + M \leftrightarrow 2O + M$	[5]	[5]	[5]
$NO + M \leftrightarrow N + O + M$	[5]	[5]	[10]
$N + e^- \leftrightarrow N^+ + 2e^-$	[6][c]	[6]	[6]
$O + e^- \leftrightarrow O^+ + 2e^-$	[5]	[5]	[5]
$N_2 + O \leftrightarrow NO + N$	[5]	[5]	[11]
$NO + O \leftrightarrow O_2 + N$	[5]	[5]	[12]
$N + O \leftrightarrow NO^+ + e^-$	[5]	[6]	[5]
$N + N \leftrightarrow N_2^+ + e$	[5]	[6]	[6]
$O + O \leftrightarrow O_2^+ + e$	[5]	[6]	[6]
$O^+ + N_2 \leftrightarrow N_2^+ + O$	[5]	[5]	[5]
$O^+ + NO \leftrightarrow N^+ + O_2$	[5]	[5][d]	[6]
$NO^+ + O_2 \leftrightarrow O_2^+ + NO$	[5]	[5]	[5]
$NO^+ + N \leftrightarrow N_2^+ + O$	[5]	[5]	[5]
$NO^+ + O \leftrightarrow N^+ + O_2$	[5]	[5]	[5]
$O_2^+ + N \leftrightarrow N^+ + O_2$	[5]	[5]	[5]
$O_2^+ + N_2 \leftrightarrow N_2^+ + O_2$	[5]	[5]	[5]
$NO^+ + N \leftrightarrow O^+ + N_2$	[5]	[5]	[5]
$NO^+ + O \leftrightarrow O_2^+ + N$	[5]	[5]	[5]
$N^+ + N_2 \leftrightarrow N_2^+ + N$	N/A	[6]	[6]
$O_2^+ + O \leftrightarrow O^+ + O_2$	N/A[e]	[6]	[6]
$N_2 + e \leftrightarrow N + N + e$	[5]	[6]	[13]
$O_2 + e \leftrightarrow O_2^+ + e$	N/A	N/A	[14]

[a] Park 93 has radiative recombination which is not calculated by DPLR

[b] In cases when the references in Johnston's publication do not agree with, or are not the original source of, the rates in Johnston's work, the reference has been corrected in this table.

[c] Park's text (i.e. Park90) is believed to contain a typographical error. The rate from Park93 is used instead.

[d] Different activation energies are given in Park's 1990 and 1993 publications. DPLR uses the rate from Park's text, even though it is likely incorrect.

[e] Park's text uses the same rate as Park93, but this rate is omitted from DPLR's .chem file due to a typographical error in Park's text.

All together, there are $2 \times 3 \times 2$ options which makes for 12 different variations in modeling options. All 12 variants are shown for selected analyses. Over a wider range of analysis, we focus on three specific modeling options. The Park90 model with $T_e=T_t$ is chosen as the baseline. Park93 and Johnston14 are examined with $T_e=T_v$. The choice of Huo vs. Park excitation rates is taken depending on spectral range, as will be discussed. In Section V, the discrepancies with existing models are examined in detail, and new models, different than any of the above options, are discussed as they are derived and presented.

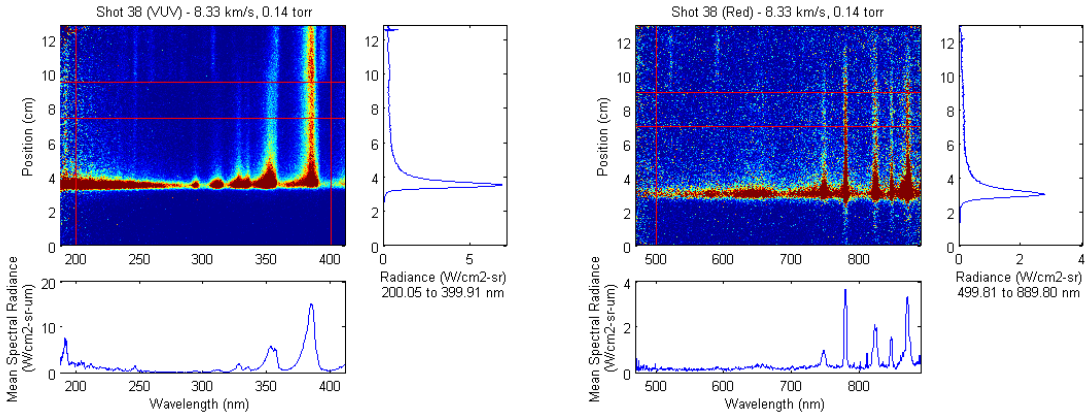

Figure 1. Sample data sets obtained in the EAST facility

IV. Results

The EAST data are obtained in the format of absolute radiance versus position and wavelength. An example data set is shown in Figure 1. The cross-section in the horizontal direction provides a spectral radiance while the vertical direction is the radiance versus position. The radiance versus position displays the non-equilibrium overshoot at the shock front and relaxation toward equilibrium. In order to quantify the non-equilibrium radiance, we have previously defined a metric as the integral of radiance within ±2 cm of the peak radiance.[15, 16] When normalized by the shock tube diameter, this would have units of radiance and is equivalent to the radiance accumulated through 4 cm of the non-equilibrium "zone" when radiation is optically thin. This non-equilibrium metric may also be calculated over spectral radiance data without performing integration over wavelength. In this case it is referred to as the spectral non-equilibrium metric. The spectral non-equilibrium metric is shown in Fig. 2 for one test condition, in order to identify spectral features. The spectral features present are summarized in Table 4. For further analysis, the data are grouped into spectral ranges. These ranges, summarized in Table 5, are determined by both the ranges of individual spectrometers and the spectral features observed.

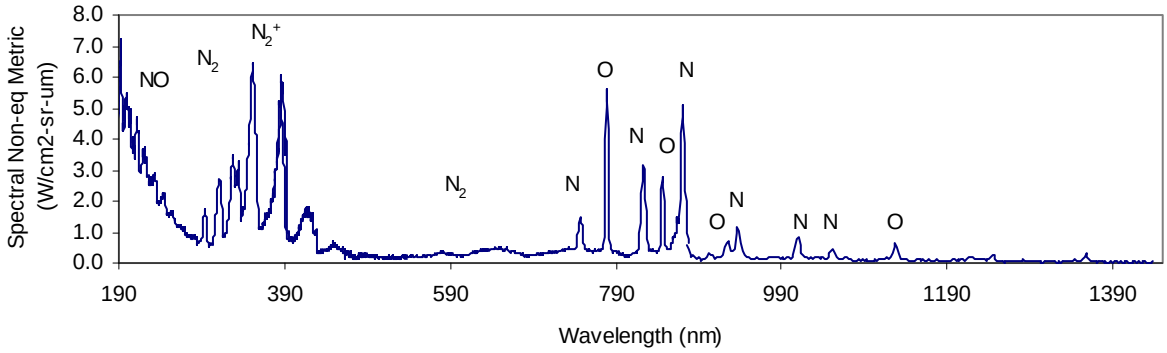

Figure 2. Non-equilibrium spectral metric at 8.33 km/s and 0.14 Torr.

With 7 different spectral regions, 12 different simulation options, and 7 different pressure/tube diameter combinations, the full comparison cannot be presented within this work. Instead, a subset consisting of the spectral non-equilibrium radiance for 4 of the test conditions in Table 1 over the full wavelength range is shown, along with the radiance versus position for 2 test conditions at 3 of the spectral ranges in Table 5. As discussed above, the Park90 model with T_e=T_t, and Park93 and Johnston14 with T_e=T_v are respectively chosen as baseline and new models for comparison of the spectral non-equilibrium metric. The radiance versus position is presented with all 12 modeling options at a limited range of pressures.

Table 4. Major spectral features in this work

Species	Feature	Transition	Major Features or Range (nm)
NO	γ, δ, ε	$(A^2\Sigma^+, C^2\Pi, D^2\Sigma^+) \rightarrow X^2\Pi$	200-300
N_2	2nd Positive	$C^3\Pi \rightarrow B^3\Pi$	337.1 357.7 380.5
	1st Positive	$B^3\Pi \rightarrow A^3\Pi$	500-750
N_2^+	1st Negative	$B^2\Sigma^+_u \rightarrow X^2\Sigma^+_g$	330.8 358.2 391.4 427.8 470.9
N		$3p\ ^4S \rightarrow 3s\ ^4P$ $3p\ ^4S \rightarrow 3s\ ^4P$ $3p\ ^4P \rightarrow 3s\ ^4P$ $3p\ ^2P \rightarrow 3s\ ^2P$ $3p\ ^4D \rightarrow 3s\ ^4P$ $3p\ ^2D \rightarrow 3s\ ^2P$	744.2 746.8 821.6 862.9 868.0 939.3
	NIR lines	$3d\ ^4F \rightarrow 3p\ ^4D$ $3d\ ^4D \rightarrow 3p\ ^4P$	1011.5 1054.0
O		$3p\ ^5P \rightarrow 3s\ ^5S$ $3p\ ^3P \rightarrow 3s\ ^3S$	777.2 844.6
	NIR lines	$3d\ ^5D \rightarrow 3p\ ^5P$ $3d\ ^3D \rightarrow 3p\ ^3P$	926.6 1128.7

Table 5. Ranges selected for analysis

Camera	Spectral Range (nm)	Features Included
UV	190-280	NO
	280-320	N_2
	320-370	N_2/N_2^+
UV/Vis	370-500	N_2^+
Vis/NIR	500-700	N_2
	700-890	N, O 3p
NIR	890-1450	N, O 3d

A. VUV/UV Wavelength (190-500 nm) comparison

The 190-500 nm region primarily consists of molecular features. Because of the lack of atomic features, atomic modeling options, such as excitation rates, have little to no impact on the spectra. Figure 3 shows the comparison of the non-equilibrium spectral metric at 4 of the pressures examined. Radiation features attributed to NO are underpredicted by all models, as are features attributed to the N_2 2nd Positive bands. Prediction of N_2^+ varies significantly with pressure. At the low-pressure conditions of 0.01 and 0.05 Torr (not shown), the N_2^+ radiation is significantly overpredicted when using T_e=T_v. Possible reasons for this overprediction will be discussed in Sect V. The heritage Park90 (T_e=T_t) approach matches the N_2^+ features at 0.01 Torr, but underpredicts radiance at higher pressures. At higher pressures, the N_2^+ radiation becomes more accurately predicted by the T_e=T_v models, agreeing well from 0.14-0.50 Torr, then becoming underpredicted at higher pressure. Some CN contamination is observed near 388 nm, particularly in the 10 cm tube at higher pressures [17, 18], but this is not accounted for in the present work. The differences between Park93 and Johnston14 models are of little consequence in this range.

a) 0.01 Torr

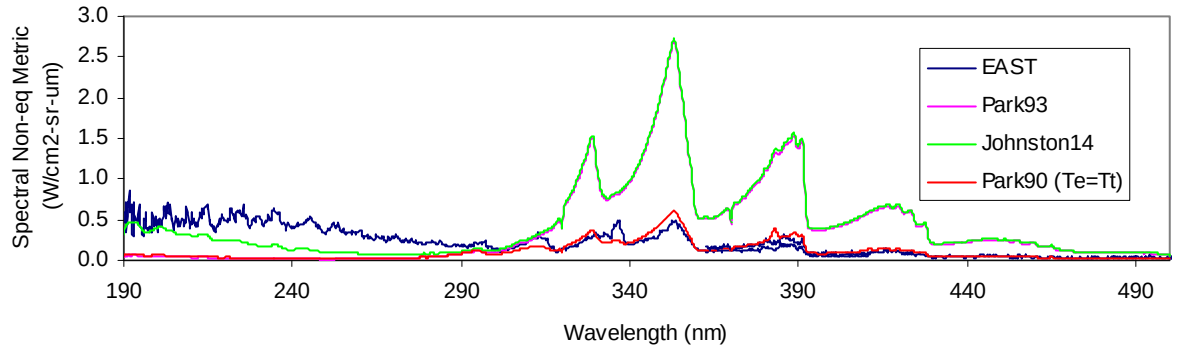

b) 0.14 Torr

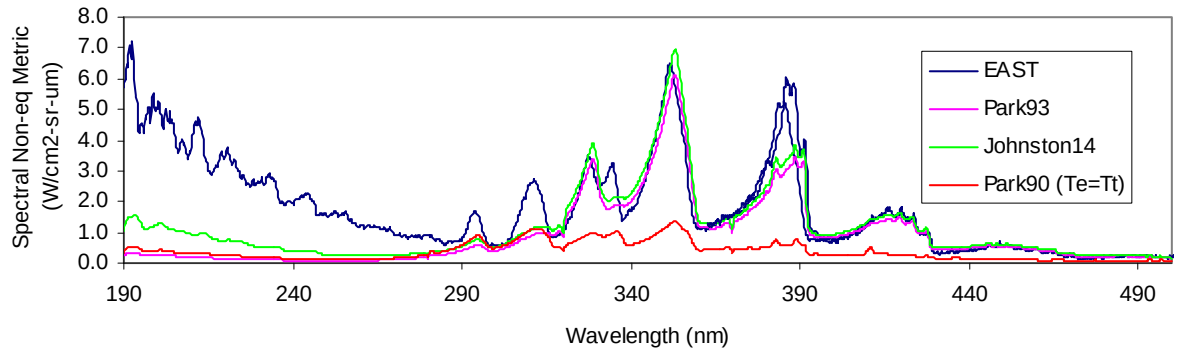

c) 0.30 Torr

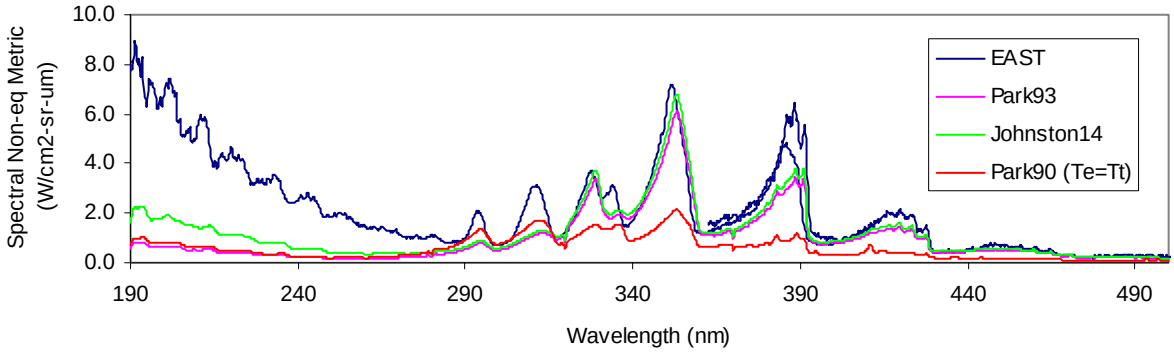

d) 0.70 Torr

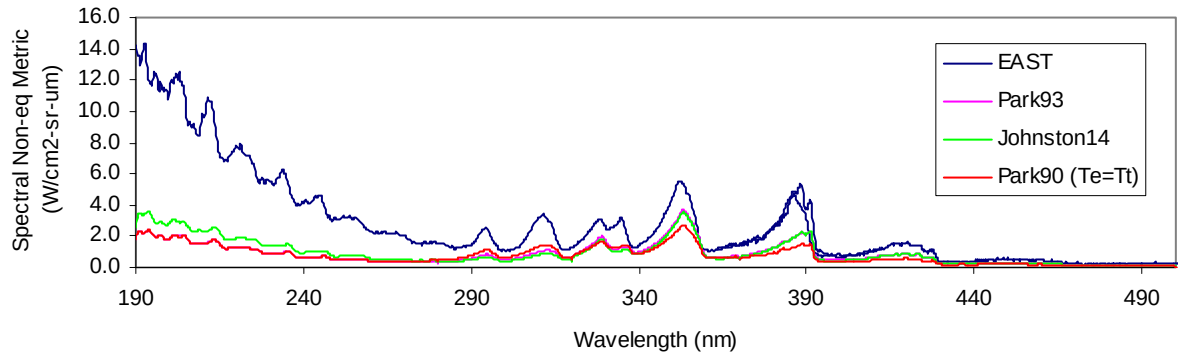

Figure 3. Spectral non-equilibrium metrics from 190-500 nm at four pressures.

The radiance versus position for two of the cases above (0.01 and 0.30 Torr) are shown for the range 320-370 nm in Figure 4, using the 12 different combinations of thermal, chemical and excitation models. The result is insensitive to excitation model because there is no atomic N present in this spectral range. The significant overprediction of N_2^+ radiance discussed above at 0.01 Torr is apparent in all T_e=T_v options. For T_e=T_t, both Park93 and Johnston14 overpredict substantially. The Park90 model, which showed good agreement in Figure 3(a), is seen not to match the spatial profile and is more sharply peaked than the data. At 0.3 Torr, the T_e=T_t models all underpredict the radiance, while the Johnston model matches the peak signal. The T_e=T_v models, while being close to the spectral non-equilibrium metric (Figure 3), are more peaked in time than the data and do not match the relaxation tail well.

a) 0.01 Torr

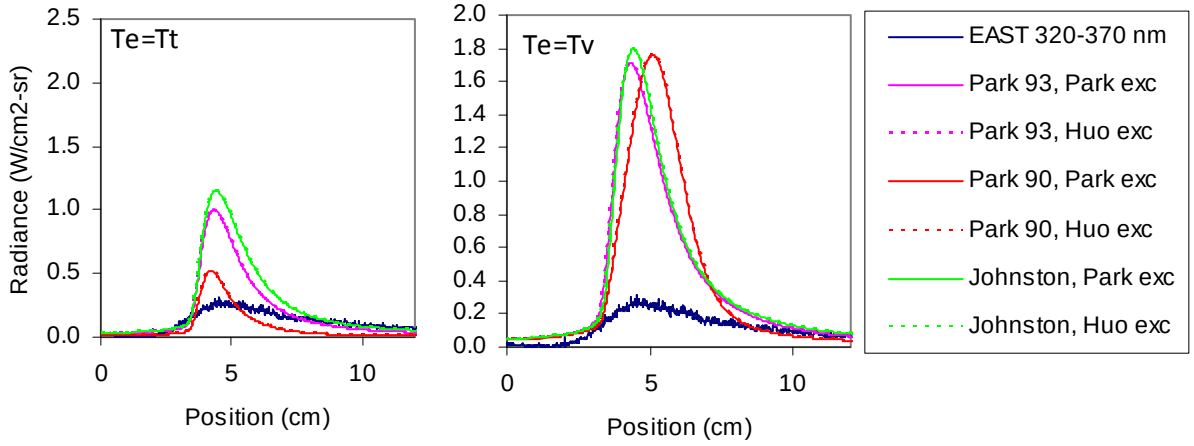

b) 0.30 Torr

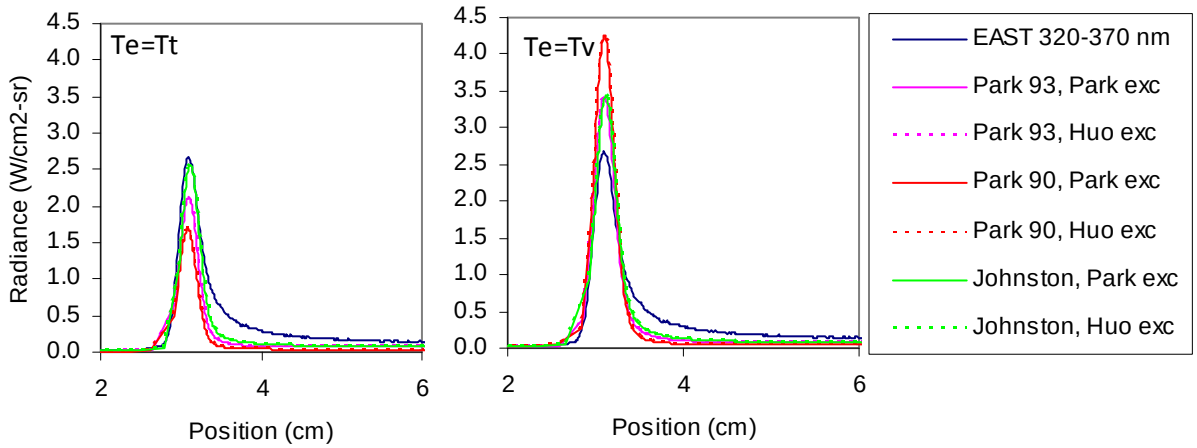

Figure 4. Comparison of radiance from 320-370 nm at pressures of 0.01 Torr (top) and 0.30 Torr (bottom).

a) 0.01 Torr

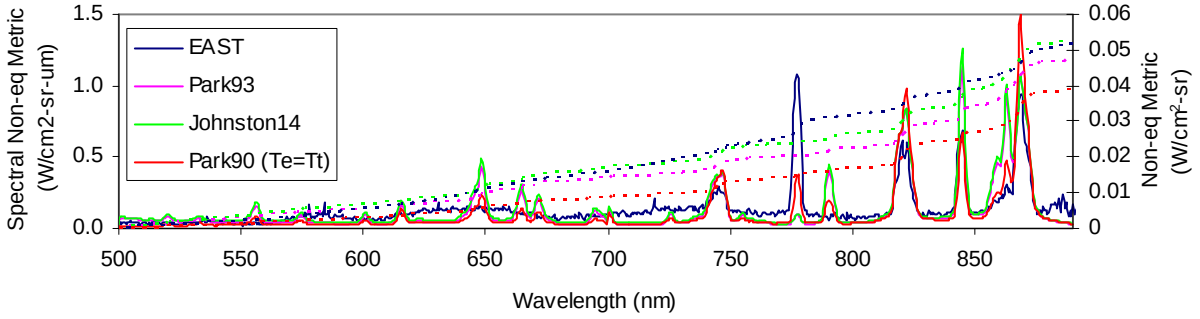

b) 0.14 Torr

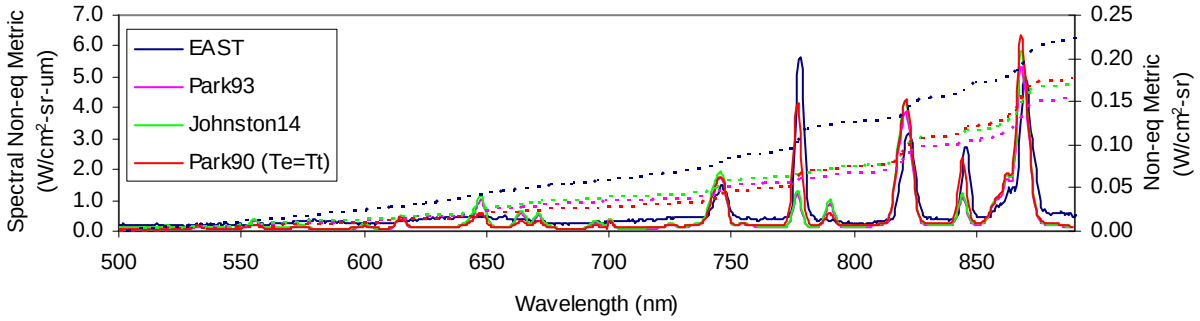

c) 0.30 Torr

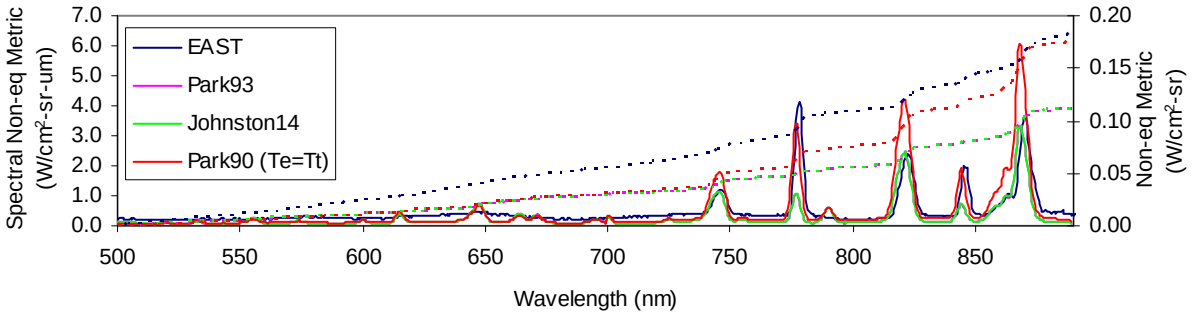

d) 0.70 Torr

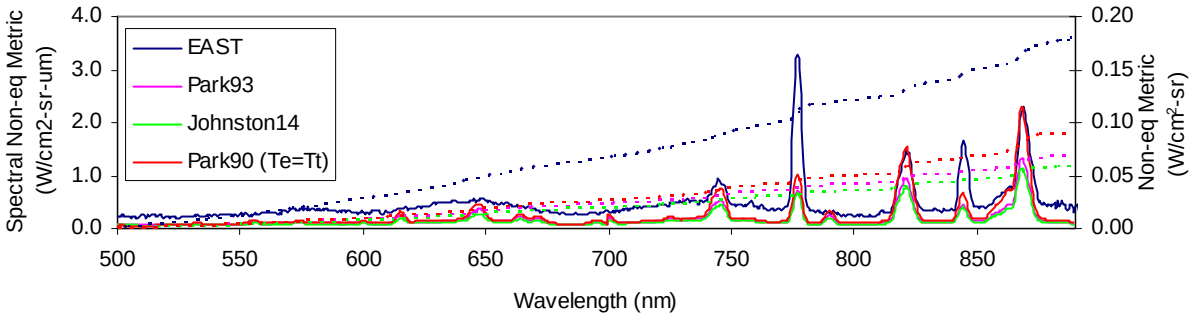

Figure 5. Spectral non-equilibrium metrics from 500-890 nm.

B. Vis/Red Wavelength (500-890 nm) comparison

The 500-890 nm region consists of N_2 molecular excitation and atomic 3p transitions. Figure 5 shows the comparison of the non-equilibrium spectral metric in this range at 4 of the pressures examined. In order to aid the comparisons, the integral of the spectral metric is shown as a dotted line. The broad feature from 500-800 nm is attributed to N_2 1st positive radiation and is not predicted by any of the models. Several atomic features are predicted in the 500-700 nm range but are not observed in experiment. These lines generally originate from 5s and higher states of N, indicating the density of upper states is overpredicted. Lines at 777 and 845 nm are attributed to 3s states of O. The 777 nm line is underpredicted by T_e=T_v models at all conditions, while the Park90 (T_e=T_t) model displays a fair match from 0.14-0.50 Torr, but underpredicts at high and low pressure. The agreement to the 845 nm line is similar to the 777 nm line at pressures above 0.14 Torr, but inverts at lower pressure, where the line is well matched by Park90 (T_e=T_t) but overpredicted by the T_e=T_v models. The 845 nm line is just slightly higher in energy than the 777 nm line, and the disagreement indicates errors in either the QSS prediction or the electronic temperature input to NEQAIR. The atomic N lines are generally overpredicted at the lowest pressure, but matched well from 0.05-0.50 Torr. At 0.70 Torr, the N lines are underpredicted by the T_e=T_v models but matched by Park90 (T_e=T_t).

a) 0.05 Torr, 8.87 km/s

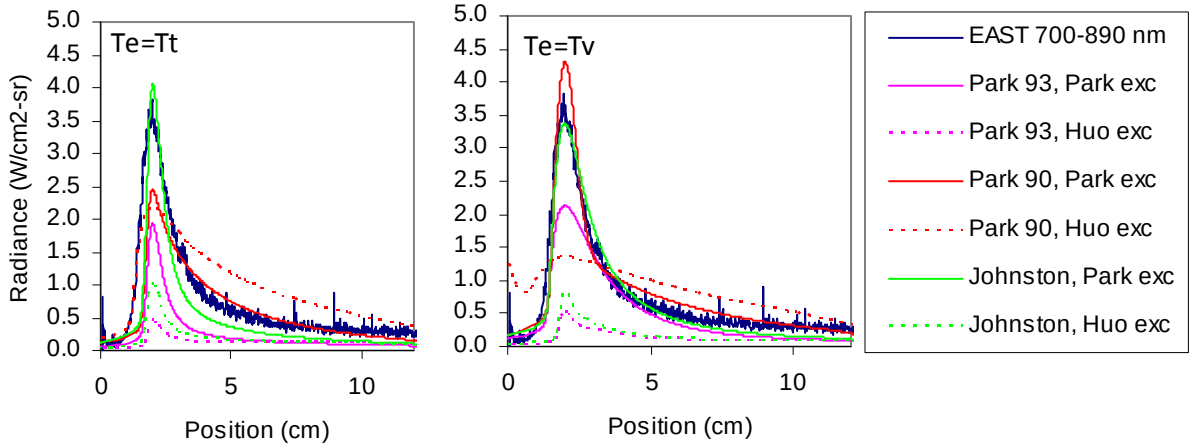

b) 0.50 Torr, 7.71 km/s

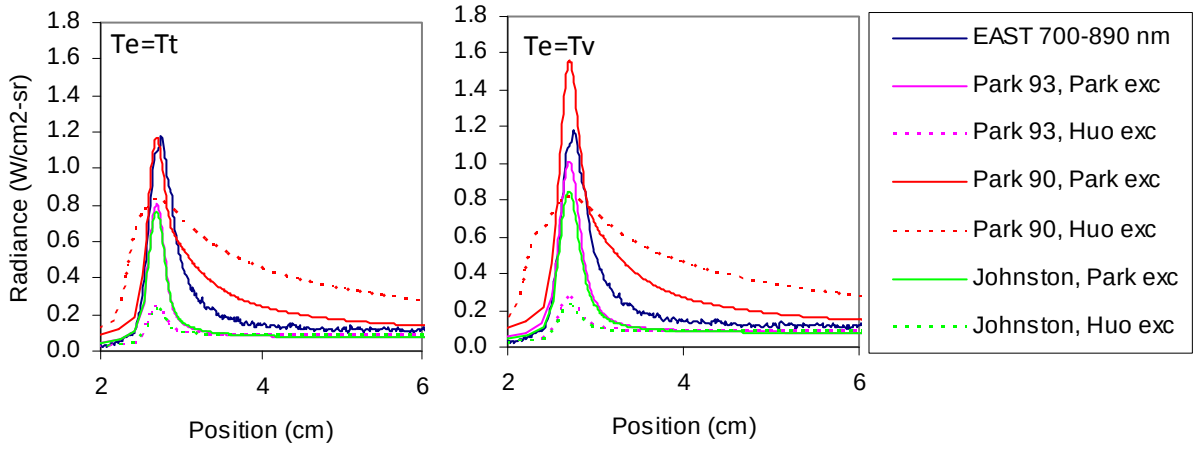

Figure 6. Radiance versus position from 700-890 nm.

a) 0.01 Torr

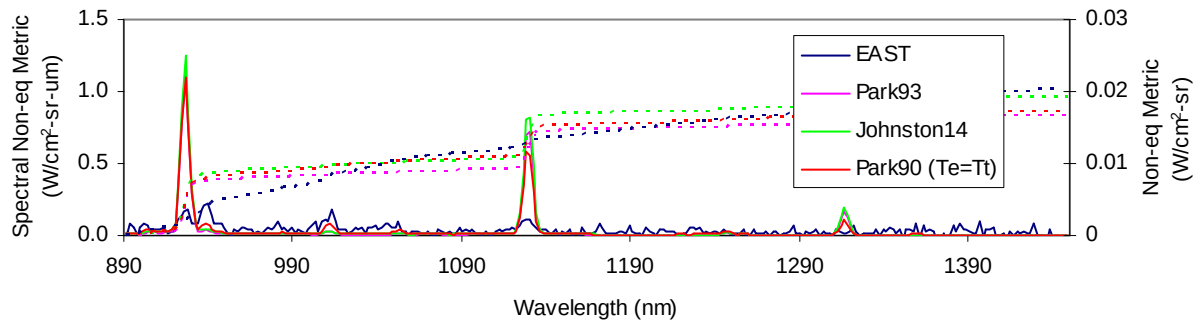

b) 0.14 Torr

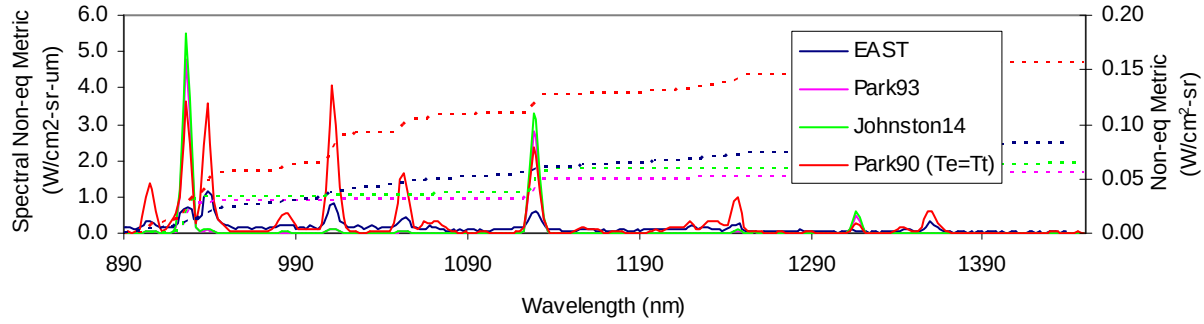

c) 0.30 Torr

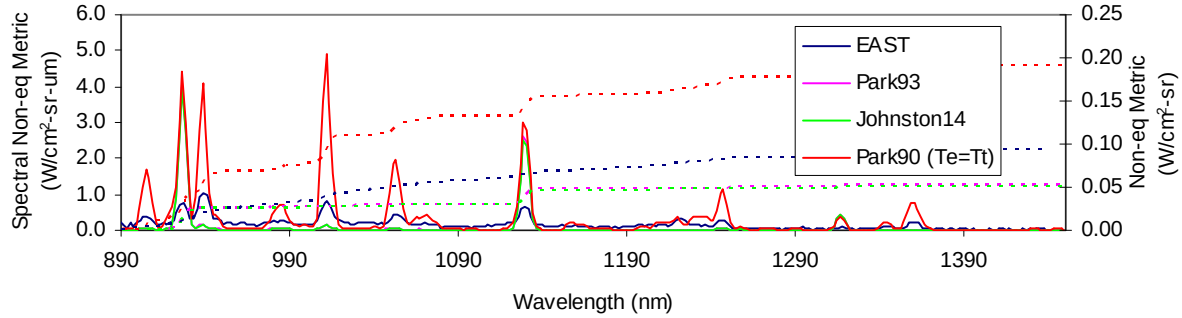

d) 0.70 Torr

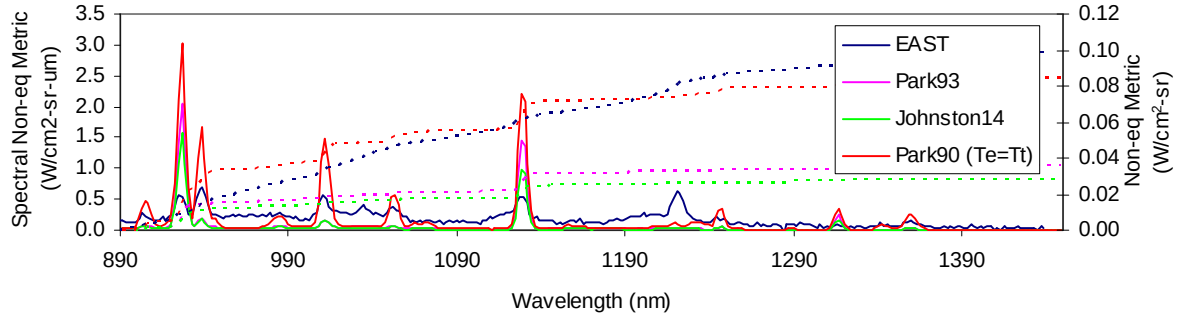

Figure 7. Spectral non-equilibrium metrics from 890-1450 nm.

The radiance from 700-890 nm versus position is shown in Figure 6 for pressures of 0.05 and 0.50 Torr. Regardless of temperature model, the Huo excitation underpredicts the radiance profile significantly. For the Park90 kinetics, the Huo excitation produces an extended decay in radiance. This is attributed to a slow equilibration of N^+ within the Park90 model, due to the absence of N_2/N charge exchange, coupled with a slow interaction between ground and excited states in the Huo model, which favors a Saha-like distribution. Given the poor agreement to experiment, the Huo results will not be discussed further for this wavelength range. At 0.05 Torr, cases with T_e=T_t underpredict the radiance or do not follow the decay profile. Of the T_e=T_v solutions, the Johnston14 model with Park excitation shows good apparent agreement with the data. Spectral data, however, show that the Johnston14 model overpredicts N atom and underpredicts O atom, to the extent that the total radiance balances. The Park93 model underpredicts the initial radiance while Park90 overpredicts. The Park93 results are observed to better predict the N atom radiance in comparison to Johnston14. At higher pressure (0.5 Torr) the differences between T_e=T_t and T_e=T_v become less distinguished, indicating that the extent of thermal non-equilibrium is diminishing at higher pressure. The Park90 model overpredicts radiance with longer decays while the Johnston14 and Park93 rates yield a narrower peak. Examination of the spectral data show that the N atom intensities are well matched and the underprediction is mainly due to the O atom and underlying N_2 molecular radiation.

a) 0.01 Torr, 8.57 km/s

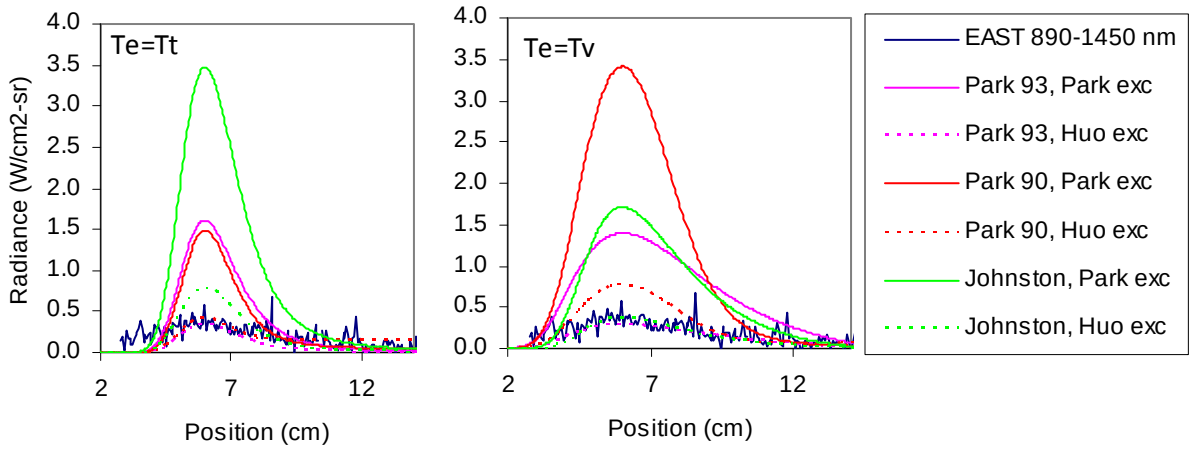

b) 0.30 Torr, 8.09 km/s

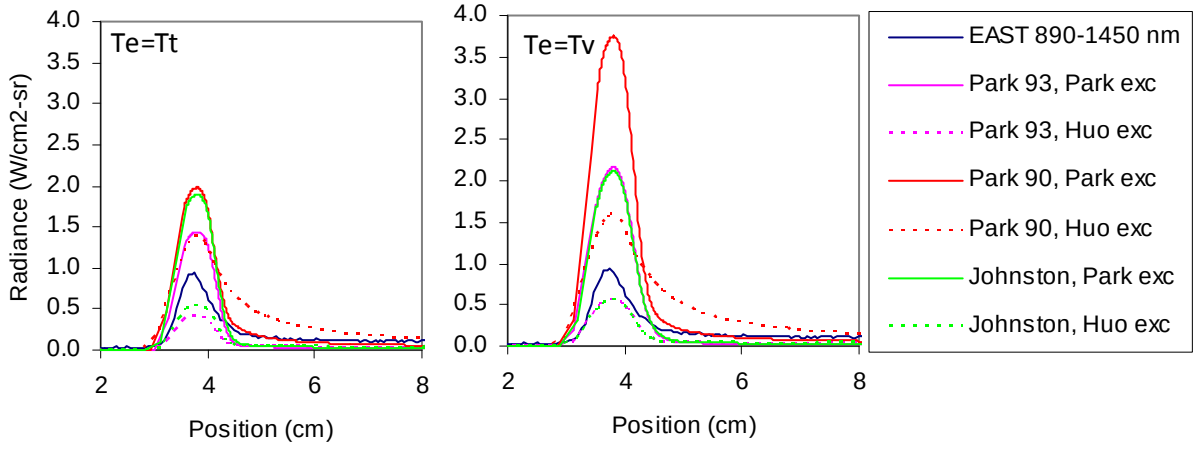

Figure 8. Radiance versus position from 890-1450 nm for two selected tests.

C. IR Wavelength (890-1450 nm) comparison

The 890-1450 nm region consists primarily of atomic 3d transitions, though one N 3p transition of significant intensity is within this range. In this range, the Park excitation model produces a substantial overprediction. The comparisons presented in

Figure 7 therefore use the Huo excitation rates. The integrated radiance is matched reasonably well by all models at 0.01 Torr, Park93/Johnston14 at 0.14 and 0.3 Torr, and Park90 at 0.7 Torr. However, the strengths of individual features are not matched. Three lines attributable to atomic O are substantially overpredicted by all models at all pressures. This compensates under prediction in other areas such that the integrated intensity agrees. The one line attributed to the N 3p state at 939 nm is under predicted with the Huo excitation rates for Park93/Johnston14, but becomes overpredicted by Park90 above 0.05 Torr. The Park excitation rates (not shown) predict this particular line better, consistent with the observations from 700-890 nm. However, the Park excitation overpredicts the intensity of the 3d states of N substantially.

The comparison of relaxation is selected at representative pressures of 0.01 and 0.30 Torr in Figure 8. Substantial overprediction at both pressures is observed with the Park excitations due to excessive radiation for 3d states. Some of the Huo excitation curves appear to agree well with the radiance curve due to offsetting errors in N and O radiation intensities. At low pressure, the curves are more sharply peaked for T_e=T_t models, while the T_e=T_v trend is more consistent with experiment.

D. Summary

A comparison of the radiance over the seven spectral ranges in Table 5 and ten shots in Table 1 is given in Table 6. These values represent the integrals of the spectral data for different bands, and are provided for purposes of quantitative comparison of the data in this work, as well as providing a metric that future developments in predictive modeling may be benchmarked against.

Table 6. Summary of Non-equilibrium metrics over the seven spectral ranges and ten shots

Shot No	Velocity (km/s)	Pressure (torr)	Tube Diameter (cm)	Spectral Range (nm)	Non-equilibrium Metric (W/cm^2-sr)			
					EAST	Park90	Park93	Johnston14
15	8.18	0.01	60.33	190-280	0.038	0.0030	0.0025	0.015
				280-320	0.0075	0.0041	0.0068	0.0084
				320-370	0.013	0.014	0.058	0.065
				370-500	0.011	0.012	0.055	0.059
32	8.57	0.01	60.33	500-700	0.015	0.0084	0.011	0.016
				700-890	0.035	0.030	0.034	0.044
				890-1450	0.020	0.057	0.080	0.11
8	8.62	0.05	60.33	190-280	0.085	0.011	0.0060	0.035
				280-320	0.022	0.014	0.018	0.029
				320-370	0.065	0.022	0.13	0.16
				370-500	0.057	0.017	0.12	0.14
24	8.87	0.05	60.33	500-700	0.036	0.017	0.029	0.042
				700-890	0.095	0.057	0.059	0.078
				890-1450	0.059	0.095	0.19	0.26
20	8.29	0.14	60.33	190-280	0.13	0.020	0.013	0.046
				280-320	0.033	0.026	0.022	0.028
				320-370	0.089	0.038	0.12	0.14
				370-500	0.081	0.029	0.11	0.12
22	8.36	0.14	60.33	500-700	0.045	0.024	0.029	0.034
				700-890	0.084	0.071	0.048	0.055
				890-1450	0.041	0.13	0.16	0.18
38	8.33	0.14	10.16	190-280	0.24	0.021	0.013	0.049
				280-320	0.047	0.027	0.024	0.031
				320-370	0.13	0.040	0.13	0.15
				370-500	0.14	0.030	0.12	0.13
				500-700	0.058	0.027	0.034	0.041
				700-890	0.16	0.15	0.12	0.14
				890-1450	0.085	0.16	0.23	0.27
42	8.09	0.3	10.16	190-280	0.31	0.041	0.032	0.074
				280-320	0.057	0.041	0.029	0.034
				320-370	0.14	0.061	0.13	0.15
				370-500	0.16	0.043	0.11	0.13
				500-700	0.055	0.030	0.029	0.031
				700-890	0.13	0.15	0.081	0.085
				890-1450	0.097	0.19	0.19	0.20
46	7.71	0.5	10.16	190-280	0.43	0.066	0.060	0.10
				280-320	0.066	0.042	0.028	0.027
				320-370	0.13	0.069	0.10	0.10
				370-500	0.14	0.049	0.089	0.093
				500-700	0.040	0.030	0.026	0.023
				700-890	0.078	0.10	0.059	0.054
				890-1450	0.10	0.18	0.13	0.11
50	7.34	0.7	10.16	190-280	0.53	0.093	0.091	0.12
				280-320	0.071	0.034	0.026	0.023
				320-370	0.12	0.063	0.074	0.072
				370-500	0.13	0.049	0.068	0.071
				500-700	0.066	0.026	0.023	0.020
				700-890	0.11	0.063	0.045	0.040
				890-1450	0.10	0.11	0.083	0.066

V. Modeling Improvements

The reported discrepancies have been examined in greater detail by investigating the modeling choices that are built into the predictions. This includes kinetic rates within the CFD code and electronic state-to-state rates employed within the radiation code. While there is interdependence on how different features in the spectrum are impacted by these choices, to first order, it is possible to examine the processes that control individual features and improve them independently, possibly iterating on the process until all features are reasonably predicted. Thus, the ensuing discussion is divided into sections depending on the species involved. The practice preferred in this work is to use the data to select from different modeling options or input parameters in the literature, rather than adjusting rate coefficients or other values to exactly agree with the data presented here. The intent is to maintain some degree of independence between input parameters and validation data. The hope is that this will lead to a model that is more broadly applicable over multiple conditions if it is not strictly tuned to match just one condition.

A. Nitric Oxide (NO)

The NO bands are universally underpredicted by DPLR/NEQAIR in this study. This indicates likely problems in the NEQAIR non-Boltzmann model for NO. To study this further, an appropriate rate model must be selected for NO. The non-Boltzmann effects should be minimized at higher pressure conditions, therefore the rate models are tested by comparing predictions based on Boltzmann distributions at 0.7 Torr to the data. Under Boltzmann distribution, the results based on Johnston rate coefficients show very good agreement with the data, while either Park model is still significantly below the data. As Boltzmann distributions typically form the upper bound for radiance in a compressive shock, this indicates that it is nigh impossible to capture the NO radiance using Park kinetic models. Rather than adopting the Johnston model outright, however, we examine the reactions that affect the NO number density. There are three important reactions controlling NO formation/dissociation. This includes the general dissociation reaction:

$$NO + M \leftrightarrow N + O + M \tag{1}$$

and the so-called Zel'dovich exchange reactions:

$$N_2 + O \leftrightarrow NO + N \tag{2}$$

$$O_2 + N \leftrightarrow NO + O \tag{3}$$

Candidate reaction rates for these three reactions are shown in Figure 9. Note that reaction (3) has been written as the reverse process in Park's work, and rates available in the literature may be obtained in either direction. For purpose of comparison, rates given for the reverse process are converted to the forward rate using equilibrium constants determined from the Chemical Equilibrium and Applications (CEA) program, and are noted as such in Figure 9.[19]

For NO dissociation (Figure 9(a)), the Park90 and Park93 models use the same rates that were fit to data from Koshi, et al.[20] Johnston used simulations based on the LAURA/HARA tool suite to adjust this reaction rate to match EAST data collected in CO_2/N_2 mixtures,[10] and found the Park rates had to be reduced by a factor of 2.5. This result yields a reaction rate very similar to that recommended in NIST reviews of combustion reaction rates by Tsang and Herron[21], based on the measurements of Thielen and Roth.[22] We have independently recommended the rate of Tsang in our analysis of the same CO_2/N_2 tests studied by Johnston[23]. The rates shown in Figure 9(a) are specifically for the case where N_2 is the non-reactive collision partner. For atoms, an enhancement factor of 22× was recommended by Park based on Koshi's study, and the same multiplier was adopted by Johnston. Tsang's review, on the other hand, recommended a multiplier less than 1 based on data collected in Argon. This multiplier will be a subject of discussion in regards to the current data below.

The Zel'dovich exchange reactions originally compiled by Park utilized data that was mostly obtained at low temperatures (2000-4000 K) and the rate coefficients were fit using arbitrarily fixed temperature exponents in the rate constant [5]. This led to very uncertain extrapolations to temperatures of interest for entry shocks. These rates were also the subject of NIST reviews of combustion reactions by Tsang/Herron[21] and Baulch, et al.[24] Bose and Candler later computed these rates using quasi-classical trajectory (QCT) simulations[12, 25], obtaining results that were more in-line with the combustion literature than the rates used by Park. Fujita[11] also analyzed the published literature on reaction (2) to obtain a rate constant that is very similar to Baulch's. In 2001, Park's updated air model[26] purportedly used the rates computed by Bose, although the rates listed in this publication are a mixture of Park90 heritage and the Bose rates. The LAURA code (as reported in Johnston 2014) adopted the Bose rate for reaction (3), and Fujita's rate for reaction (2).

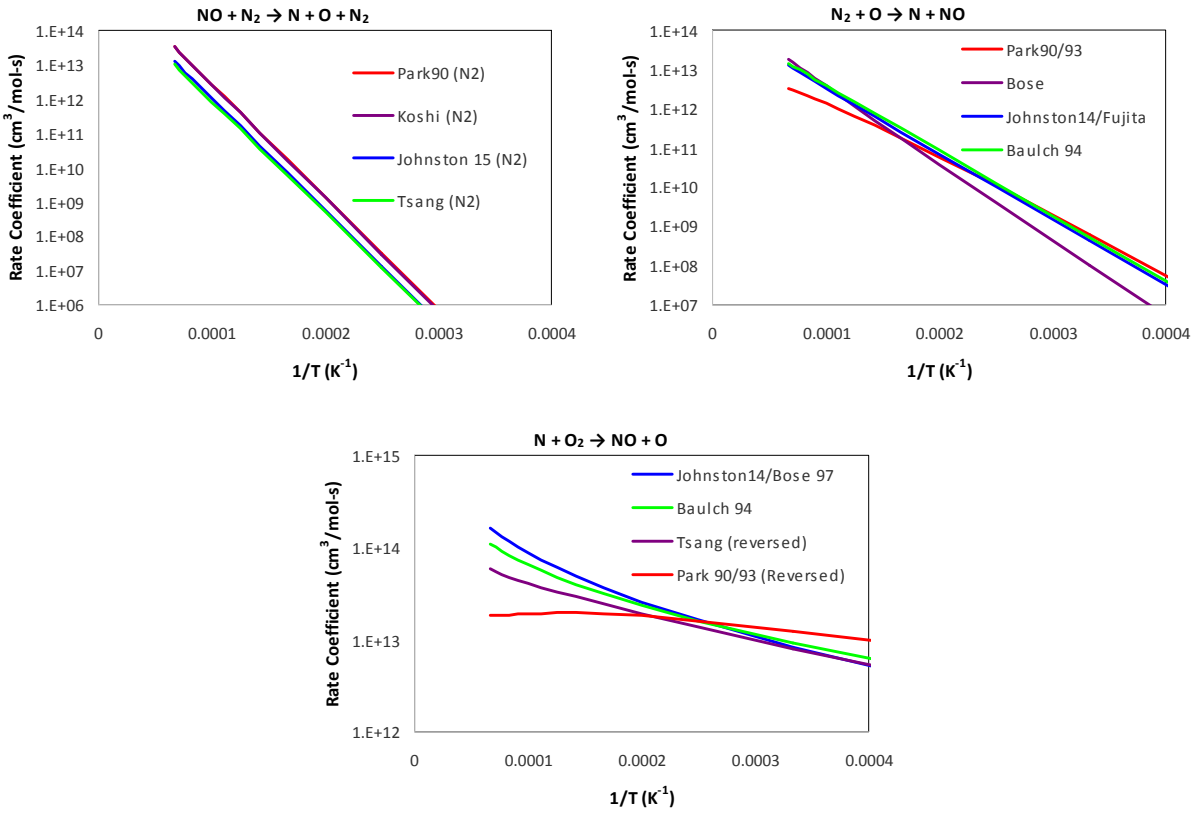

Figure 9. Rate coefficients for the three major NO reactions

The comparison of NO number densities along an equivalent 1D stagnation line for the 0.7 Torr case with different reactions is shown in Figure 10. Oxygen atoms generated from the rapid decomposition of O_2 cause reaction (2) to be the primary mechanism for NO creation in the initial part of the shock wave. Reaction (3) is significant, but of somewhat lower importance. The effect of changing the Zel'dovich reactions are shown as "Park 93 + Exchange", where the use of Bose's Zel'dovich rates increases the NO concentration at the shock front substantially, in line with that found with Johnston's chemistry. While the equilibrium of reaction (2) favors the formation of NO over N_2, the NO is formed in quantities that exceed its equilibrium mole fraction. Thus, reaction (1) destroys the NO that is created via exchange, and therefore controls both the peak NO concentration and the relaxation toward an equilibrium NO density. Reducing this rate, as in the Johnston14 chemistry, causes a slower reduction of NO density. If the rate of reaction (1) due to atomic collision partners is reduced to be equal to the rate from molecular partners, the NO concentration is increased further and the decay is protracted as shown by the curve marked "kAtom=kMolec."

The analysis of Boltzmann radiation shows that the NO density must be at least at the level predicted by the Johnston14 model, thus it is necessary to alter all three of these reactions in accordance with the aforementioned data sources. We therefore choose the rates selected through review of the combustion literature (i.e. Ref [21, 24]) for reaction (1) (with M=N_2) and for reactions (2) and (3). The appropriate rate to use with atomic collision partners cannot be greater than that employed by Johnston, but may be less depending on the choice of non-Boltzmann modeling parameters. This consideration will factor into the evaluation of NO non-Boltzmann modeling which is discussed next. It is noteworthy that all models examined before have neglected any dissociation of NO due to impact with electrons. This is examined further below.

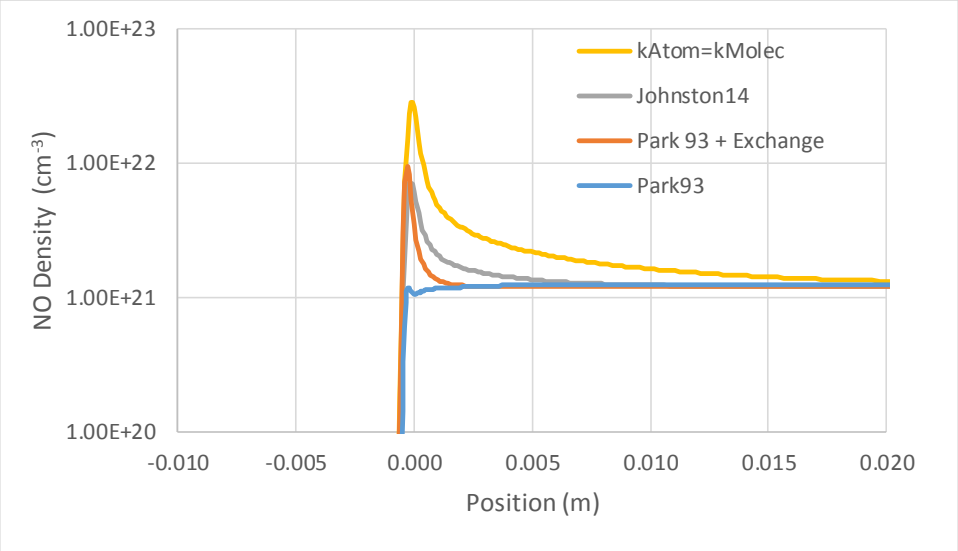

Figure 10. NO Number Densities predicted at 0.7 Torr with different reaction rates

The non-Boltzmann modeling of NO in NEQAIR performs a mole balance on excited states of the NO molecule based on radiative transitions, excitation and de-excitation between states due to electron and heavy particle collision, and NO dissociation and recombination due to spontaneous (i.e. predissociation) and collisional (electron and heavy) processes. The relative rates and data sources of these different processes were examined and updated. For these conditions, it is found that the concentration of states responsible for NO band radiation is determined by the balance between dissociation and internal excitation rates, and is primarily controlled by heavy particles, i.e.

$$NO(X) + M \leftrightarrow NO(A,C,D) + M \quad (4)$$

$$NO(A,C,D) + M \leftrightarrow N + O + M \quad (5)$$

These processes, as implemented in NEQAIR, have been examined previously with respect to the BSUV experiment as reported by Levin, et al.[27] In the case of BSUV, reaction (5) was nearly in equilibrium and determined much of the radiative spectrum. For the present work, if reaction (5) were brought into equilibrium, the radiance would be even lower than the existing predictions. Thus, in order to explain the current data, reaction (5) must be far from equilibrium and reaction (4) should be larger in a relative sense.

NEQAIR's default rates for heavy particle excitation (4) are treated identically for all molecules, depending only upon the difference in energy between states. Fundamental rate data for heavy particle excitation of excited molecular states is non-existent, however the reverse of process (4) is quenching, which has been measured for many molecular states. Comparison of the quenching rates inferred from NEQAIR's excitation model to quenching rates in the literature shows that it is about an order of magnitude too low. The heavy particle impact rates for NO were therefore replaced with rates based on quenching, the forward rate being inferred by the inverse process. Rates for the A, B and a states were primarily obtained from the model of Cartry [28], which is built for room temperature plasma processes. Much of Cartry's data came from the study of Raiche [29], who measured quenching as a function of temperature and found it varied only with the collision frequency, i.e. as $\sqrt{T}$. The quenching rate therefore is given by:

$$k_q = k_{q,0}\sqrt{\frac{T_t}{300}} \quad (6)$$

Values used for k_{q0} for several states of NO are given in Table 7. Specific values for these rates are given for collision partners of O_2, NO, and N_2. For other species, an order of magnitude is assigned that is similar to those obtained for the three collision partners. For N_2 collisions with the A state, significantly lower quenching rates have been observed, but increase with temperature. The data from Thoman, et al. [30] has been fit with an Arrhenius dependence to determine this rate. Data from Asscher and Haas [31] were used for the D state, but rescaled so that their rates for the A state match that of Cartry. Data for the b and C states were not available, so assumed the same as the a and B states, respectively. For most cases, the quenching rate given is a total quenching rate, i.e. is the sum of relaxations to all other states of the molecule. In the absence of more specific data, we have assumed that the quenching branches equally to all lower states of the molecule, i.e.

$$k_q\left(n \to m\right) = \frac{k_{q,n}^{tot}}{n-1} \tag{7}$$

where n is the state's position in the energy ordered list of NO states. Values of n are given in the first column of Table 7. One exception to this is the transition (D→C) which was specifically determined by Laux[32] for atomic collision partners. This value (given in footnote to Table 7) is therefore subtracted from the overall quenching rate before normalizing as in (7).

Table 7. Quenching rates adopted for electronic states of NO

Energy Order, n	Name of State	Quenching Rate @ 300, k_{q0} (s^{-1})			
		N_2	O_2	NO	Others
1	X	N/A	N/A	N/A	N/A
2	a	1.19×10^{-11}	4.27×10^{-11}	1.38×10^{-10}	1.0×10^{-10}
3	A	*	1.5×10^{-10}	2.0×10^{-10}	1.0×10^{-10}
4	B	6.1×10^{-13}	1.5×10^{-11}	2.0×10^{-10}	1.0×10^{-10}
5	b	1.19×10^{-11}	4.27×10^{-11}	1.38×10^{-10}	1.0×10^{-10}
6	C	6.1×10^{-13}	1.5×10^{-11}	2.0×10^{-10}	1.0×10^{-10}
7	D	4.83×10^{-11}	4.57×10^{-10}	3.31×10^{-10}	1.0×10^{-10} †

* The formula $k_q = 3.6 \times 10^{-13} \exp(-1430/T) + 2.42 \times 10^{-11} \exp(-10180/T)$ is used instead of equation (6).
† For atoms and D→C, $k_{q0} = 2.49 \times 10^{-10}$ s^{-1}.

The rate of reaction (5) in NEQAIR is based upon very early studies by Park [33], and involved an Arrhenius rate constant whose pre-factor is consistent with the overall dissociation rate of the molecule. Different pre-factors are used for atomic and molecular collision partners. The dissociation energy of the particular electronic state is taken as the activation energy. With the revisions to the NO dissociation rate discussed above, it became prudent to update these rates to be consistent with the dissociation rate being recommended. In contrast to the prior implementation, however, we insist that the expected molecular dissociation rate be matched when the molecular population is Boltzmann distributed, i.e.:

$$k_{diss} = \frac{1}{q}\sum k_{d,n} q_n^{vr} e^{-E_n/T_e} \tag{8}$$

which is realized by setting:

$$k_{d,n} = \frac{q k_{diss} e^{-D_n/T}}{\sum q_n^{vr} e^{-D_n/T} e^{-E_n/T_e}} \tag{9}$$

At this point, the only parameter for NO radiation that is not independently defined is the relative ratio of dissociation due to molecular and atomic collisions. The predicted non-equilibrium metric using different ratios for this value is shown in Figure 11(a). For this purpose, the same ratio is applied in both NEQAIR and DPLR. It is seen that a ratio of 5 most adequately reproduces the data at 0.7 Torr. This same model is also applied to the data at 0.01 Torr [Figure 11(b)] and is found to match the data reasonably well. The impact of some other adjustments to the kinetic model, discussed further in Sect. VI, are also shown in Figure 11(b). The mismatch at low wavelength is mostly due to the NO ε band, which originates from the D state of NO. While the camera noise is significant in this range, it seems likely the non-Boltzmann population of this state is being overpredicted at low pressure.

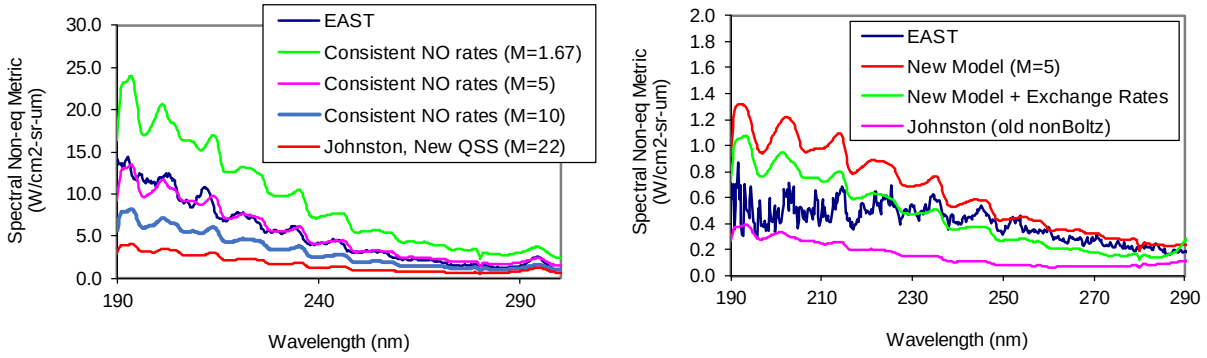

Figure 11. Non-equilibrium NO radiance with different parameters. (a) Impact of changing relative atom/molecular dissociation rates for NO at 0.7 Torr. (b) Applicability of revised model at 0.01 Torr.

The above discusses only the parameters that had major impact upon the prediction. Several other parameters and calculation methods in NEQAIR's molecular non-Boltzmann routine were updated during this process, and will be documented in a future publication or technical note. These include the electron impact excitation and dissociation rates, the introduction of state-specific exchange rates, and the method of evaluating the electron impact excitation and dissociation in regards to the ro-vibrational distribution of the molecule. One noteworthy result of these methods was the evaluated magnitude of electron-impact dissociation of NO. NEQAIR has historically approximated the electron impact dissociation cross-section of NO as equivalent to the excitation cross-section measured by Imami[34]. When this rate is integrated over a Maxwellian electron energy distribution and summed over all states of the molecule, the effective electron impact dissociation rate obtained is 3800 times larger than the molecular heavy particle impact rate. Although the electron density is low at these conditions, this rate is large enough as to be non-negligible. This rate is adopted and carried forward into the kinetic model summarized in Section VI. This is expected to be an improvement over the existing practice, where electron impact dissociation of NO is set to zero. The exclusion of this rate in earlier studies may explain why the atom to molecule ratio needed to be as large as 22 and is inconsistent with newer data. Considering the approximate nature of this derivation, however, this rate should be re-examined in the future. Electron impact dissociation of NO is generally known to proceed through dissociative attachment, forming N and O^-. Cross-sections for this process are much larger [35] than that employed in NEQAIR, and the energy threshold is lower, meaning that this rate may be significantly higher than the aforementioned estimate. Including this rate in the CFD calculation may allow the ratio of NO dissociation due to molecular and atomic collision to be reduced even further.

B. Nitrogen (N_2)

Like NO, the Nitrogen radiation was underpredicted at all conditions studied in this work. The updates that were made in the course of improving the NO model (including changes to chemical kinetics and the computation of electronic-state specific dissociation/excitation rates) by themselves resulted in significant improvement in the underprediction. The heavy particle impact rates for Nitrogen were next updated to be consistent with quenching rates in the literature for N_2, as summarized in Table 8.[36-38] Introduction of quenching rates caused the N_2 1st positive prediction to be well matched at 0.7 Torr, but the 2nd positive radiation was now overpredicted, as the C state was pulled into a Boltzmann distribution by the increased internal excitation rates. Electron impact excitation and dissociation rates were then revised within the molecular QSS. Errors were discovered in NEQAIR's electron impact calculations, some of which date back to its original implementation [39], and these calculations were reformulated as described in the Appendix. Upon correcting the electron impact rates and updating the dissociation cross-sections to match those recommended by Itikawa [40], a new electron impact dissociation rate was determined for N_2 using the dissociation rate predicted from NEQAIR. This rate is shown in Figure 12 along with electron impact dissociation rates determined by Park[5], Sharma[41], and Bourdon[13]. These three rates are those used in the Park 90, Park 93 and Johnston 14 models, respectively. The rate is seen to lie between the two Park rates and that employed by Johnston. Because this rate is based on reliable cross-sections and computed consistently in NEQAIR, we carry this rate through to the CFD rate model as given in Table 9. Further refinements to Nitrogen modeling in CFD were undertaken. The Millikan-White rates for N_2-N relaxation were updated in accordance with Grover, et al. [42] with no noticeable impact. The N_2 dissociation rates derived computationally and reported by

Jaffe and co-workers[43] were tested. Altering the N_2 dissociation rate could move the entire spectrum (i.e. both 1st and 2nd positive) up (using QSS rates) or down (with thermal rates) and thus it was possible to obtain a better fit of one band or the other depending on which rate was used. However, the Park determined N_2 dissociation rates were best on average for reproducing the data. It has been suggested that the C state of N_2 responsible for the second positive radiation may be equilibrated with the atom densities due to pre-dissociation[44], however at this condition the radiance would be much too low if this were the case. Some lowering of the C state density (and, hence, 2nd positive radiation) may be realized were a pre-dissociation rate introduced for the C state, however this is not done at this time as studies of pre-dissociation in the C state suggest this does not occur except for $\nu > 5$.[45] These vibrational levels, however, are unbound and not included in NEQAIR's level model.

Table 8. Quenching Rates adopted for electronic states of N_2

Energy Order, n	Name of State	Quenching Rate @ 300, k_{q0} (s^{-1})					
		N_2	O_2	NO	N	O	Others
1	X	N/A	N/A	N/A	N/A	N/A	N/A
2	A	3.0×10^{-16}	2.1×10^{-12}	6.9×10^{-11}	2.0×10^{-12}	2.1×10^{-11}	1.0×10^{-11}
3	B→X	1.0×10^{-12}	4.0×10^{-11}	1.0×10^{-10}	1.0×10^{-10}	1.0×10^{-10}	1.0×10^{-10}
	B→A	1.5×10^{-11}	1.0×10^{-10}	2.4×10^{-10}	1.0×10^{-10}	1.0×10^{-10}	1.0×10^{-10}
4	A	1.9×10^{-13}	2.8×10^{-11}	3.6×10^{-10}	1.0×10^{-11}	1.0×10^{-11}	1.0×10^{-11}
5,6	C,C'	2.9×10^{-11}	3.1×10^{-10}	1.0×10^{-10}	1.0×10^{-10}	1.0×10^{-10}	1.0×10^{-10}

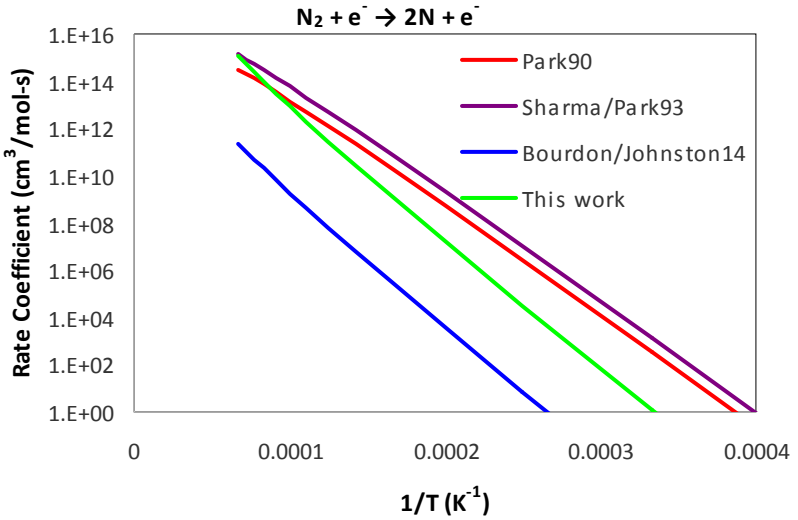

Figure 12. Electron impact dissociation rates for Nitrogen

C. Nitrogen Cation (N_2^+)

The N_2^+ First Negative system is predicted well at the higher pressure condition, but becomes substantially over-predicted at lower pressures. The Park90 model with T_e=T_t appears to predict the average non-equilibrium spectrum well (Figure 3(a)) but examination of the spatial profile (Figure 4(a)) shows the agreement to be mostly fortuitous. Examination of the non-Boltzmann calculation shows that N_2^+ is predicted to be in a Boltzmann distribution, even at 0.01 Torr. This fast equilibration in the electronic distribution of N_2^+ is attributed mostly to the large internal excitation cross-section taken from the work of Crandall[46]. This experimentally determined cross-section appears supported by calculations as well[47], so it is difficult to justify modifying or discarding it, though some previous studies have done exactly that. Other state specific processes for N_2^+ were examined, but none were identified that could conceivably result in a non-Boltzmann distribution of N_2^+ at our test condition. Thus, we turn our attention to the flowfield solution and reaction mechanisms. N_2^+ is formed in the shock primarily by the associative ionization process:

$$N + N \longleftrightarrow N_2^+ + e^- \tag{10}$$

The rate used by Park in 1990 was taken as a mean of several data sets in the reverse direction (thereby matching none of them), then calculated in the forward direction by detailed balance. The temperature exponent was fixed at zero. This exponent was re-considered in Park's 1993 work, leading to the rate that is used presently in both Park93 and Johnston14. As it happens, the Park rate shows good agreement with rates computed using newer cross-section data for the reverse process.[48] The newer data infers somewhat higher rates of reaction at relevant temperatures, so would serve to worsen the agreement if adopted.

Park's publication had recommended the rate for associative ionization be controlled by the geometric mean temperature $\sqrt{TT_v}$. Current implementations of LAURA and DPLR, however, require this temperature to be controlled by the translational temperature T_t. This practice arises from the logical argument that the energy of a collision between neutral species is driven by the translational energy. The reverse process, involving electron impact collision, may be thought to be driven by T_e. This reverse controlling temperature, however, favors the forward reaction in the non-equilibrium region as $T_e < T_t$. Literature on the reverse process of (10) (dissociative recombination) shows that product atoms are produced preferentially in electronically excited (metastable) states[49]. Detailed balance therefore requires that the forward process be dominated by reactions involving metastables. This creates a dependence of the forward reaction rate upon T_e. We examine the dependence of N_2^+ concentration on controlling temperature for T_t, $\sqrt{T_tT_e}$ and T_e in Figure 13(a). It is seen that the peak N_2^+ density is reduced and relaxation time is increased as the temperature control shifts toward T_e. This occurs because the N_2^+ density follows the same trend as the temperature controlling its formation. The experimentally observed radiance attributed to N_2^+, as seen in Figure 4, is overlaid on Figure 13(a) and correlates well with the density obtained when electronic temperature is controlling. The impact to non-equilibrium radiation is shown in Figure 13(b). Although the radiance appears correlated to the N_2^+ density in its decay profile, the magnitude of the radiance is not well matched. This is because the radiance depends on both temperature and number density. Explanations for the discrepancy require further investigation.

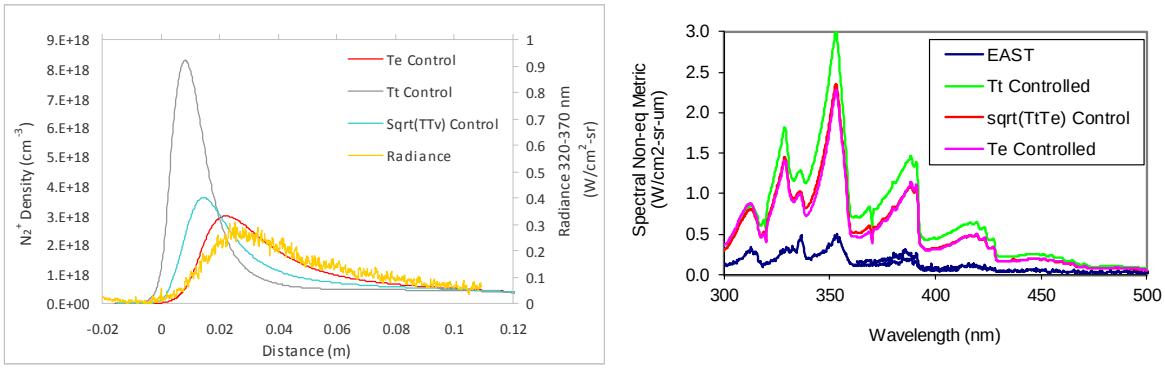

Figure 13. (a) Variation in N_2^+ with different controlling temperatures for associative ionization. (b) Corresponding non-equilibrium radiance for the three cases.

D. Atomic Nitrogen and Oxygen

Radiation from atoms showed varying degrees of success, with more highly excited states (3d and above) being substantially overpredicted, and the 3p states being relatively close. Changes to rate chemistry, as discussed in the preceding sections, have some impact on atomic radiation, but appears to be secondary to the internal excitation rates that control the non-Boltzmann population of atomic levels. The heavy particle impact rates recommended by Lemal, et al.[50] were adopted in NEQAIR14, so are included in the predictions of Sect. IV. For the present conditions, these rates appear less critical than the electron impact rates. The electron impact rates in NEQAIR14 are based upon the rates recommended by Park in the original implementation of NEQAIR[5]. However, several of these rates have been adjusted (i.e. reduced by 1-3 orders of magnitude) over the years such that the lineage of NEQAIR's atomic non-Boltzmann model is no longer well documented. Recently, Huo conducted an evaluation of electron impact rates for N, O, and C atoms[8], and these rates were tested for the current cases. The rates provided by Huo were found to reduce all atomic radiation substantially, which was desirable for the higher atomic states, but not 3p states. The state distribution for the peak radiance point at the 0.7 Torr case is shown in Figure 14. The 3s, 3p and 3d energy regions are labeled on the plot. The Park model places 3d states near the Boltzmann level, which causes the overprediction of radiance in the infrared. The Huo model promotes equilibration between most upper states of the molecule, which suppresses the population of both 3p and 3d states while raising the population of states near the ionization limit. This causes the observed reduction in radiance.

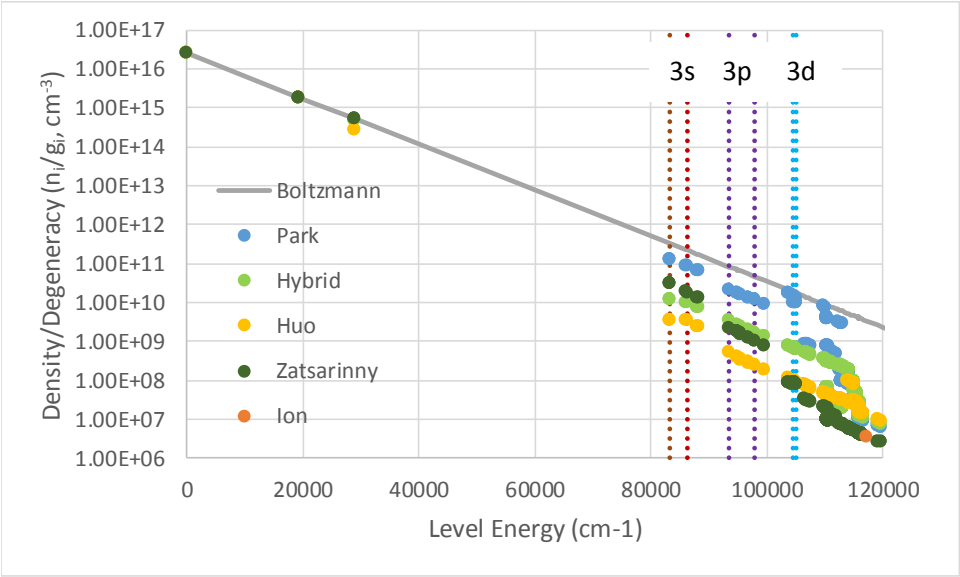

Figure 14. Distribution of excited N atom states with different internal excitation models

A hybrid model was created by combining Huo's rates for dipole allowed transitions with Park's rates for unallowed transitions. Doing so reduced the equilibration of the n=3 states with states near the ionization limit, as seen in Figure 14. At the same time, the 3d states are brought into equilibrium with the 3s and 3p states and no longer sit at the Boltzmann level. The hybrid Park/Huo model is thus expected to better reproduce the data than either model alone. Two additional sets of rates based on the Drawin formula and calculations by the group of Zatsarrinny[51, 52] were provided by Lopez and Panesi[53] and were also tested. The results from these two sets of rates were fairly similar, therefore only the results based on Zatsarinny are shown. These rates cause the 3d and higher states to equilibrate with the ionization limit, with the 3p and 3s being progressively closer to the Boltzmann population, but not equilibrating with each other.

The impact of the electron impact excitation model in terms of atomic radiation is shown in Figure 15(a). The integrated radiance is below the EAST radiance for all cases. The Park model clearly overpredicts lines in the infrared so must be discarded even though it is closer in terms of overall intensity. The Huo and Zatsarinny based predictions yield similar levels of radiance in spite of differences in state populations. The Huo/Park hybrid rates are slightly higher than Zatsarinny or Huo without overpredicting the data, so are carried for further study at present. Rates for this combined model are shown in Table 10 through Table 13, following the formula originally employed in NEQAIR by Park:

$$k_{mn} = C\left(\frac{T_e(K)}{10,000}\right)^n e^{-\Delta E/T_e} \tag{11}$$

Earlier versions of NEQAIR contained a normalization factor based upon the principal quantum number of the states involved in the transition. This normalization can be embedded in (or removed from) C so it is no longer carried. The rates given are based upon the level lumping scheme employed in NEQAIR and documented by Park.[5] The data that has informed the new rates, however, is not based on lumped levels. These rates are thus converted to an effective lumped level rate based upon a Boltzmann weighting of all states within the groups:

$$k_{mn} = \frac{\sum_{i\in m,\, j\in n} k_{ij}(T_e) g_i e^{-E_i/T_e}}{\sum_{i\in m} g_i e^{-E_i/T_e}} \tag{12}$$

where i, j are the specific states involved and m, n are the lumped states.

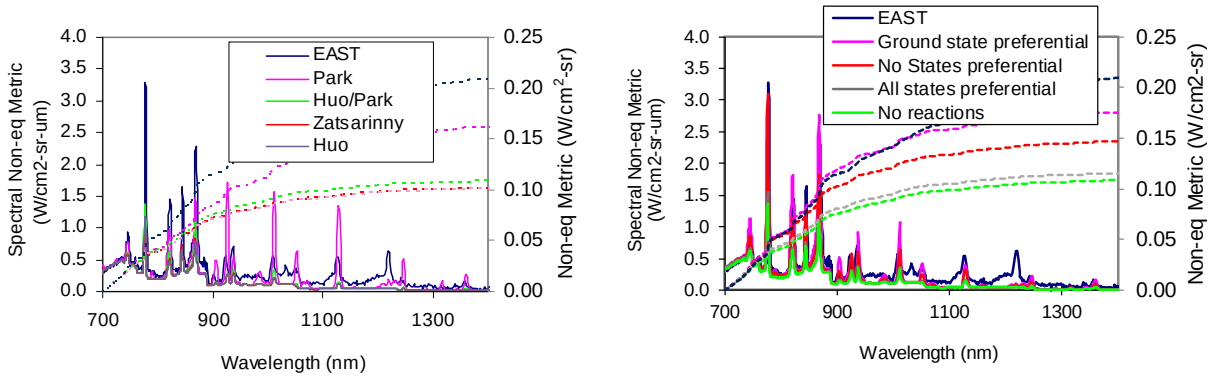

Figure 15. Comparison of non-equilibrium radiance from atomic lines at 0.7 Torr, as predicted by (a) different internal excitation models and (b) different associative ionization model assumptions.

A larger impact to atomic radiation may be realized by introducing additional processes into the atomic non-Boltzmann model. Traditional non-Boltzmann modeling of atomic radiation balances internal excitation and radiation processes with ionization, and adjusts ground state concentration to match the flowfield input (quasi-steady state assumption). Often, the rate of ionization is small compared to other reaction processes and the adjustment required under quasi-steady state is substantial. If reaction processes involve excited atomic states, this may produce significant error. The non-Boltzmann model has therefore been modified to include associative ionization (equivalently, dissociative recombination) and exchange processes. Rather than attempting a DMS or QCT simulation, which would require potential energy surfaces for all electronic states of the reacting system, state-specific rate coefficients are estimated, using the difference in energy between the states involved to create an Arrhenius relation. The temperature dependent pre-factors are assumed proportional and are normalized so as to sum to the correct overall reaction rate for a Boltzmann distribution. Preference factors for different combinations of states may be applied to this treatment. For exchange, the preferred atomic products for any given pair of excited electronic states can be determined by examining the molecular energy diagrams and identifying the state of the expected dissociation products. The energies involved in exchange are generally much lower than the energy of the emitting atomic states, and this process primarily impacts the non-Boltzmann solution for the metastable levels. For dissociative recombination, preferred products from the ionic ground state have been measured and are available in the literature.[54-57] For dissociation from the excited states of molecular ions, no such data is available. We show the impact of three different assumptions for the preference of dissociative recombination in Figure 15(b). Introducing dissociative recombination with no state preference (i.e. rate is only a function of the energy difference) increases the intensity of the 3p lines significantly, to the point where they are in good agreement with the measurement. If the literature values for preferences in dissociation of the molecular ion ground state are introduced, but excited states retain no preference, the radiance is increased further, showing even closer agreement to the data. If the excited states are assumed to retain the same preference as the ground state, on the other hand, the radiance is reduced and becomes comparable to that obtained when dissociative ionization is not included. The proper solution should lie somewhere between these last two cases. For the moment, we proceed with having preference for ground state, but not excited state, dissociation. It is noted that this modeling may have a meaningful impact on N_2^+ radiation, were the results of the atomic non-Boltzmann calculation fed into the molecular non-Boltzmann computation. Presently, the molecular non-Boltzmann populations are calculated assuming the atomic states are Boltzmann distributed.

VI. Revised Model Performance

With the corrections discussed above, the agreement to the data is re-examined. For these purposes, the kinetic model outlined in Table 9 is employed. The rate model builds upon the 1993 model recommended by Park.[6] Many of the rates for that study (and its predecessor) are retained, as they have been in similar studies. The particular rates that have been revised include the NO dissociation rate and exchange reactions discussed in Sect. V.I.A, and N_2 electron impact dissociation as discussed in Sect. V.I.B. Besides that, some important exchange processes have been updated or added based on review of literature. The rate of charge exchange between N and N_2 has been revised by integrating the cross-section measurements of Phelps.[58] This replaces the rate from ref. [6] which was only approximate and not based on any data. Charge exchange between NO and N was recently identified by Higdon, et al., as a key controlling reaction for determining shock temperature and number densities[59], yet this reaction has traditionally been overlooked in the existing models. The exact source of the rate employed in the aforementioned study is difficult to identify, hence it has been re-evaluated here by integrating the cross-sections obtained by Moran, et al.,[60] approximating the cross-section as constant with respect to collision energy. This yields the value given in Table 9.

Table 9. Revised rate model for hypersonic entries in air

Reaction	M	A (cm^3/mol·s)	n	E_a (K)	Controlling Temperature	Ref
$N_2 + M \rightarrow 2N + M$	Molecule	7.0×10^{21}	-1.6	113,200	$\sqrt{TT_{ev}}$	[5]
	Atom	3.0×10^{22}				
	e^-	1.2×10^{7}	2.69		T_e	This work
$O_2 + M \rightarrow 2O + M$	Molecule	2.0×10^{21}	-1.5	59,500	$\sqrt{TT_{ev}}$	[5]
	Atom	1.0×10^{22}				
$NO + M \rightarrow N + O + M$	Molecule	1.5×10^{15}	0	74,570	$\sqrt{TT_{ev}}$	[21]
	Atom	7.3×10^{15}				This work
	e^-	5.7×10^{18}			T_e	This work
$N + e^- \rightarrow N^+ + 2e^-$		2.5×10^{34}	-3.82	168,600	T_e	[6]
$O + e^- \rightarrow O^+ + 2e^-$		3.9×10^{33}	-3.78	158,500	T_e	[5]
$N_2 + O \rightarrow NO + N$		1.8×10^{14}	0	38,249	T_t	[24]
$O_2 + N \rightarrow NO + O$		9.0×10^{9}	1.0	3,270	T_t	[24]
$N + O \rightarrow NO^+ + e^-$		8.8×10^{8}	1.0	31,900	T_e	[6]
$N + N \rightarrow N_2^+ + e$		4.4×10^{7}	1.5	67,500	T_e	[6]
$O + O \rightarrow O_2^+ + e$		7.1×10^{2}	2.7	80,600	T_e	[6]
$N^+ + N_2 \rightarrow N_2^+ + N$		7.0×10^{6}	1.47	13,130	T_t	This work
$O^+ + N_2 \rightarrow N_2^+ + O$		9.1×10^{11}	0.36	22,800	T_t	[5]
$O_2^+ + O \rightarrow O^+ + O_2$		4.0×10^{12}	-0.09	18,000	T_t	[6]
$O^+ + NO \rightarrow N^+ + O_2$		1.4×10^{5}	1.9	26,600	T_t	[6]
$NO^+ + O_2 \rightarrow O_2^+ + NO$		2.4×10^{13}	0.41	32,600	T_t	[5]
$NO^+ + N \rightarrow N_2^+ + O$		7.2×10^{13}	0	35,500	T_t	[5]
$NO^+ + O \rightarrow N^+ + O_2$		1.0×10^{12}	0.5	77,200	T_t	[5]
$O_2^+ + N \rightarrow N^+ + O_2$		8.7×10^{13}	0.14	28,600	T_t	[5]
$O_2^+ + N_2 \rightarrow N_2^+ + O_2$		9.9×10^{12}	0	40,700	T_t	[5]
$NO^+ + N \rightarrow O^+ + N_2$		3.4×10^{13}	-1.08	12,800	T_t	[5]
$NO^+ + O \rightarrow O_2^+ + N$		7.2×10^{12}	0.29	48,600	T_t	[5]
$NO + N^+ \rightarrow NO^+ + N$		1.8×10^{12}	0.57	0	T_t	This work

The comparison at the lowest pressure, 0.01 Torr, is shown in Figure 16 over the three spectral ranges. Spectral non-equilibrium metric is given first, followed by the radiance versus position over the corresponding wavelength range. The results with the three different rate models and Park excitation model are shown for comparison. At the low wavelength condition, the revised model overpredicts N_2 and N_2^+ and NO ε radiation, but the portion of the

spectra that is dominated by NO β is well matched. The spatial profile is not matched near the peak signal but is matched later in the decay process. The spectrum from 500-890 nm shows a better agreement to the background signal due to improvement in the N_2 first positive modeling, and the spurious atomic lines are eliminated. The 3p atomic lines are now underpredicted. The integrated radiance is, as a result, underpredicted by the revised model. The atomic lines in the infrared, on the other hand, are more closely matched, with the integral of radiance being in near perfect agreement. The radiance profile versus position is also more closely matched, although both the 500-890 and 890-1450 ranges show a sharp peak near the shock front that is not observed in the experiment. These peaks are attributed to specific atomic O lines that appear to be predicted incorrectly at the shock front. Further examination is required to resolve this and additional remaining discrepancies.

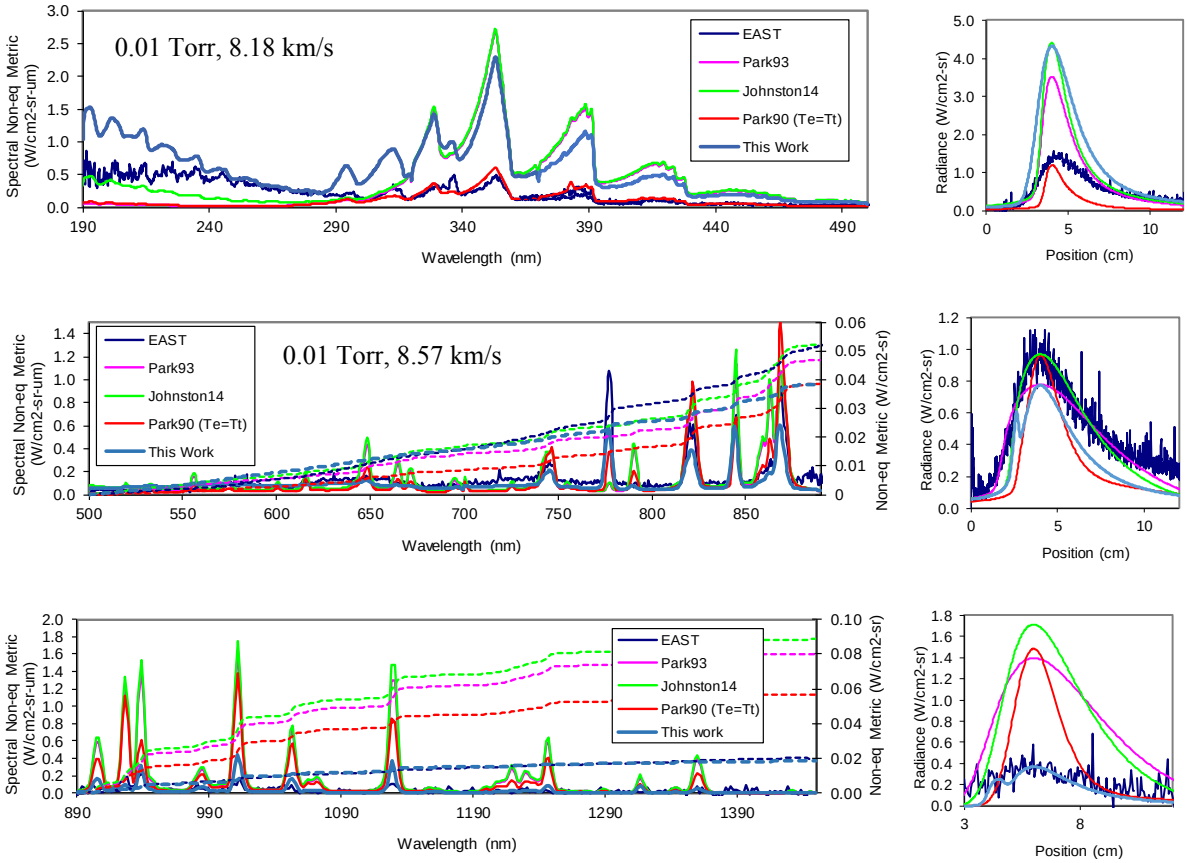

Figure 16. Comparison of Spectral non-equilibrium metric and radiance versus position as measured and predicted. Conditions: 0.01 Torr, 8.18 and 8.57 km/s.

Comparison of the new model to the high pressure (0.7 Torr) condition is shown in Figure 17, with the same manner of plots as described for Figure 16. The ultraviolet molecular radiation is no longer underpredicted, though there is some overprediction of N_2 2nd positive radiation. The profile of radiance versus position in this wavelength range is more closely matched than with the previous models. In the visible/near infrared region of 500-890 nm, the background N_2 radiance is now predicted well with no spurious atomic lines below 700 nm. The atomic lines are predicted to good accuracy, with the integrated radiance being just slightly lower than experiment. The profile of radiance versus position in this region is closely followed by the prediction. The infrared (890-1450 nm) region is underpredicted due to molecular band systems in the IR that have not been included in the present work, though the atomic lines are now more closely matched than before. The overall agreement to data is greatly improved by these adjustments, however further discrepancies remain and will be investigated further in future work.

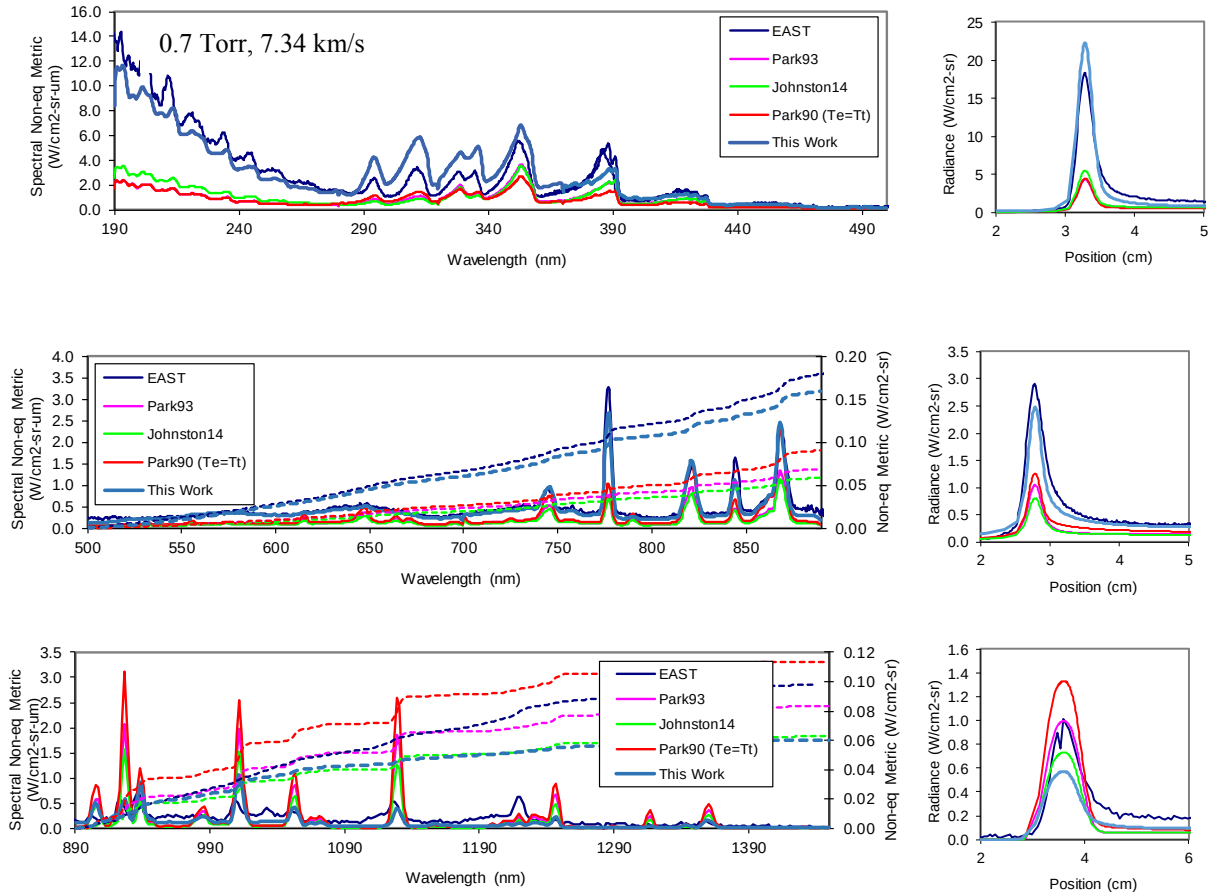

Figure 17. Comparison of Spectral non-equilibrium metric and radiance versus position as measured and predicted. Conditions: 0.7 Torr, 7.34 km/s.

VII. Summary

Comparisons of non-equilibrium radiance at shock speeds from 7-9 km/s and pressures from 0.01-0.70 Torr have been presented. Ten shots from a 51-shot test series were selected as representative cases, though data from only five of them are shown in the paper. The full set of data is available through data.nasa.gov.[3] Comparisons are first presented in terms of a non-equilibrium spectral metric, which is the integral of radiance over a 4 cm length, 2 cm in front of the shock to 2 cm behind the shock, normalized by shock tube diameter. The profile of radiance versus position is shown for selected wavelength ranges.

The experimental results are compared against predictions by the DPLR and NEQAIR codes using twelve different modeling options by varying the two-temperature model, reaction kinetics and internal excitation rates. The comparison focuses on radiation from NO, N_2, N_2^+ and atomic N and O. The salient points from the comparisons are:

1. The NO and N_2 radiation is underpredicted by all models at all conditions.
2. N_2^+ radiation is overpredicted at low pressure when T_e=T_v. N_2^+ radiation is predicted well at low pressure with the heritage model (Park 90 and T_e=T_t) but is better matched by either Park93 or Johnston14 kinetics and T_e=T_v at intermediate pressures (0.14-0.50 Torr). At higher pressures, the N_2^+ non-equilibrium is underpredicted by all models.
3. Atomic line radiation predictions are mixed. The lowest energy states of N (3p) are predicted well from 0.05-0.50 Torr when T_e=T_v is employed. The 3p states of atomic O are overpredicted by the T_e=T_v models but

[3] https://data.nasa.gov/docs/datasets/aerothermodynamics/EAST/datasets/Test_59/Test59Release.zip

predicted well at intermediate pressure ranges by the heritage model. Higher energy N and O lines, however, are overpredicted.

4. The excitation rates recommended by Huo and implemented in NEQAIR were found to underpredict most atomic features.

The causes of the discrepancies are investigated in more detail and used to derive new models for non-equilibrium air radiation, including modifications of both kinetic rates used to predict the flowfield properties and the state specific rates used in NEQAIR to predict electronic state distributions. Reaction rates involving NO, including dissociation and exchange, had to be altered to explain the observed NO radiance. Rates were altered in accordance with combustion literature. Rates for electron impact dissociation of NO and N_2 were also updated, along with charge exchange between N/N_2 and N/NO. It is suggested that the controlling reaction for associative ionization should be T_e rather than T_t which is more commonly employed. Remaining discrepancies were addressed through improvements to the NEQAIR non-Boltzmann model. Introducing new heavy particle excitation rates based on available quenching data resolved much of the disagreement in the molecular band predictions. The overprediction of N_2^+ radiation at low densities was examined but is as of yet unresolved. The controlling temperature for associative ionization was examined as a source of the overprediction. The decay profile of N_2^+ radiation suggests that this rate should have some dependency upon T_e. Atomic radiation was examined in terms of the electron impact excitation reactions, and several different electron impact rate models were examined. The rate currently adopted is a combination of NEQAIR legacy rates and selected rates from Huo. These rates eliminated spurious radiation from highly excited levels, however the lower levels were still underpredicted. It was shown that including associative ionization/dissociative recombination in the atomic non-Boltzmann model could account for some of the overprediction, however the result is very much dependent upon assumptions made regarding branching ratios for dissociative recombination.

There are a number of discrepancies remaining that will be the subject of future investigation. These include the overprediction of N_2 second positive radiation at all pressures and N_2^+ first negative and NO ε band radiation at low pressures. These are suspected to be overpredicted due to incomplete knowledge of molecular non-Boltzmann parameters. Better data on pre-dissociation rates and heavy particle impact excitation and dissociation may serve to improve the predictions. Additional band systems in the infrared (>900 nm) are observed but not modeled. The exact band systems remain to be identified and implemented in NEQAIR. The atomic line radiation is somewhat underpredicted at low pressure, with a radiation spike at the shock front that is not observed experimentally. Resolution of this difference may require better understanding of the relative importance of the states involved in associative ionization. An additional factor that has not been examined is the impact of escape factor calculation on the data, which has been shown to have relevance for non-Boltzmann populations of CN in shock-tubes[61], for instance. It is expected that these details will be refined in future study, however the present work provides an improved methodology for evaluating radiation in air shocks, and must be tested over a wider range of conditions.

Appendix

A. Electron Impact Excitation

The electron impact rates for molecules within NEQAIR are based on Park's[5] equations 2.20-2.23:

$$
\begin{aligned}
k &= \frac{\sum_{v,v'} S_{vv'} q_{vv'} e^{-E_v/T_v}}{Q_{vr}} \\
S_{vv'} &= 5.47\times10^{-11} n\sqrt{T_e(K)}\, e^{-\Delta E_{ve}/T_e} I \\
I &= \int_0^\infty (2J)^2 \exp\left[-\left(\frac{B_e' - B_e}{T_e} + \frac{B_e}{T_r}\right) J^2\right]\left(C + B\frac{B_e' - B_e}{T_e} J^2\right) dJ \\
C &= \frac{\Delta E_{ve}}{T_e} B + A
\end{aligned}
\tag{A1}
$$

A and B are constants of integration:

$$A = \int_0^\infty \frac{\sigma(\xi T_e)}{\pi a_0^2} e^{-\xi} \xi d\xi$$
$$B = \int_0^\infty \frac{\sigma(\xi T_e)}{\pi a_0^2} e^{-\xi} d\xi \tag{A2}$$

Note that, in contrast to Park's text, a dependence of A and B upon T_e is obtained through the cross-section dependence. This is because the cross section is a function of energy, E, and the T_e must be carried through with the change of variables that converted E to ξ. Earlier versions of NEQAIR did account for this, however the temperature was held at 300K. This was presumably done because the cross-section is measured with the neutral temperature at 300K. This is incorrect as the temperature in the expression is T_e, which originates from the change in variables. The physical reason for this is because the functional dependence of the cross-section is upon the electron, not neutral, energy. Corrections for the cross-section being measured at 300K will be discussed below.

Returning to the equations (A1), a specific solution for the integral is given in Park's text, and is applied in NEQAIR for cases where $B_e' > B_e$. However, in other cases the integral is evaluated as an integral over finite bounds, but the limits for integration are not well documented. Reasons for limiting the integral may be understood through considering the derivation of the integral. The integral is an approximation for a summation over rotational states. The integration to infinity assumes that the integrand vanishes before any bound on quantum number J is reached. There are three bounds to consider for the quantum number J, not all of which were implemented in earlier versions of NEQAIR. The first two have to do with the dissociation limits of the electronic state under consideration, i.e.

$$B_e' J_{\max}^2 = D_e' - E_v'$$
$$B_e J_{\max}^2 = D_e - E_v \tag{A3}$$

Neither of these bounds were considered in earlier versions. These two bounds may be combined to give:

$$J_{\max} = \sqrt{\min\left(\frac{D_e' - E_v'}{B_e'}, \frac{D_e - E_v}{B_e} \right)} \tag{A4}$$

The third bound is obtained when the rovibrational states cross over in energy, such that the lower state (v,J) becomes higher in energy than (v',J'). This bound was calculated incorrectly in earlier versions. The correct bounds are found by determining when the transition energy becomes zero. In terms of the variables in eq. (A1), this is written as:

$$J_{inv} = \sqrt{\frac{\Delta E_{ve}}{B_e - B_e'}} \tag{A5}$$

It is worth noting the ΔE_{ve} can be negative, if a cross-over in the vibrational sequence occurs. In either case, J_{inv} only exists if the term in the square root is positive. Technically, this is not a bound to the integration, as electron-impact will still cause transitions from (v,J) to (v',J'). It is, however, necessary to consider that the threshold energy may not become negative and must be fixed at zero above this limit. The threshold energy is given by:

$$E_{th} = \Delta E_{ve} + \left(B_e' - B_e \right) J^2 \tag{A6}$$

and appears twice in eq (A1). The integral is now divided into two parts, depending on whether the transition has an activation energy or not:

$$S_{vv'} = 5.47 \times 10^{-11} n \sqrt{T_e(K)} \left(I_1 + I_2 \right)$$
$$I_1 = \int_{J_{1,\min}}^{J_{1,\max}} (2J)^2 \exp\left[-\frac{\Delta E_{ve}}{T_e} - EJ^2 \right] \left(C + B \frac{B_e' - B_e}{T_e} J^2 \right) dJ$$
$$I_2 = \int_{J_{2,\min}}^{J_{2,\max}} (2J)^2 \exp\left[-\frac{B_e}{T_r} J^2 \right] A dJ \tag{A7}$$
$$E = \frac{B_e' - B_e}{T_e} + \frac{B_e}{T_r}$$

The selection of J_1 and J_2 are dependent upon the sign of ΔE_{ve} and the value of J_{inv}. The rules for determing the bound of integration are as follows:

- For $\Delta E_{ve} > 0$, $J_{1,\min}$ is zero

- If J_{inv} exists and is lower than J_{max}, and $J_{1,max}=J_{2,min}=J_{inv}$ and $J_{2,max}=J_{max}$.
- Otherwise, $J_{1,max}=J_{max}$ and $I_2=0$.

- For $\Delta E_{ve}<0$, $J_{2,min}$ is zero
  - If J_{inv} exists and is lower than J_{max}, and $J_{2,max}=J_{1,min}=J_{inv}$ and $J_{1,max}=J_{max}$
  - Otherwise, $J_{2,max}=J_{max}$ and $I_1=0$.

The integrals I_1 and I_2 may be solved in a similar fashion to Park's text, yielding incomplete gamma functions of order 1.5 and 2.5, as long as E>0. These solutions are now given as:

$$
\begin{aligned}
I_1 &= \frac{2}{E^{3/2}} \mathrm{e}^{-\frac{\Delta E_{ve}}{T_e}} \left\{ C\left[\gamma\left(\frac{3}{2}; y_{\max}\right) - \gamma\left(\frac{3}{2}; y_{\min}\right)\right] + BD\left[\gamma\left(\frac{5}{2}; y_{\max}\right) - \gamma\left(\frac{5}{2}; y_{\min}\right)\right]\right\} \\
I_2 &= 2A\left(\frac{B_e}{T_r}\right)^{-3/2}\left[\gamma\left(\frac{3}{2}; z_{\max}\right) - \gamma\left(\frac{3}{2}; z_{\min}\right)\right] \\
D &= \frac{B_e{}' - B_e}{ET_e} \\
y_{\min/\max} &= EJ^2_{1,\min/\max} \\
z_{\min/\max} &= EJ^2_{2,\min/\max}
\end{aligned}
\tag{A8}
$$

The solution for I_1 is problematic if E < 0. This introduces a complex number in the denominator and the numerical evaluation of the gamma function may be invalid. NEQAIR has a function ai3 which numerically evaluates the integral:

$$
ai_3\left(a; x\right) = \int_0^x z^a \, \mathrm{e}^z \, dz \tag{A9}
$$

By change of variables and substitution, the gamma functions may then be replaced by:

$$
\begin{aligned}
\gamma\left(\frac{3}{2}; -x\right) &= -ia i_3\left(\frac{1}{2}; x\right) \\
\gamma\left(\frac{5}{2}; -x\right) &= i a i_3\left(\frac{3}{2}; x\right)
\end{aligned}
\tag{A10}
$$

This imaginary number cancels the -i factor created by the $E^{-3/2}$ term, leading to a positive, real solution. The function may therefore being evaluated, ignoring the imaginary number, and taking the absolute value of both E and the term in brackets. The $\gamma(3/2)$ and $\gamma(5/2)$ terms will have opposite signs and should be summed prior to taking the absolute value.

In 1998, Pierrot, et al., suggested that the eq. (A1) contains an extra factor of 2J.[62] The extra factor originates from weighting the cross-section by the degeneracy of the upper state, in addition to the lower state. The weighting factor follows from assuming that the excitation cross-section to each state is identical. If degenerate states are to be included within this assumption, it would be necessary to weight the rate by the degeneracy of the product state. Without passing further judgment on the correctness of this factor, it is retained in the present work. Removal of this factor would reduce the order of the gamma functions and powers in the energy terms of eq. (A8) by 1/2.

The final consideration is the correction for cross sections being measured at 300K. If we assume the cross-section used is an overall cross-section, the cross-section will contain similar weightings as in eq. (A1), without the terms originate from integration over the electron energy distribution. This yields:

$$
\sigma_{300}\left(E\right) = \frac{\sum_{v,v'} q_{vv'} e^{-E_v/300}}{Q_{vr}(300)} n \int_0^\infty \left(2J\right)^2 \exp\left[-\left(\frac{B_e}{300}\right)J^2\right] \sigma_0\left(E - \left(E_v - E_{v=0} + B_e J^2\right)\right) dJ \tag{A11}
$$

Neglecting the dependence of σ_0 on threshold energy, we approximate:

$$
\sigma_{300}\left(E\right) = \sigma_0 \frac{n\sum_{v,v'} q_{vv'} e^{-E_v/300} \int_0^\infty \left(2J\right)^2 \exp\left[-\left(\frac{B_e}{300}\right)J^2\right] dJ}{Q_{vr}(300)} = \sigma_0 \frac{2n\Gamma\left(1.5\right)}{Q_{vr}(300)} \sum_{v,v'} q_{vv'} \left(\frac{B_{e,v}}{300}\right)^{-3/2} e^{-E_v/300} \tag{A12}
$$

This changes the reaction coefficient:

$$k = 5.47\times10^{-11}\sqrt{T_e(K)}\,\frac{Q_{vr}(300)}{Q_{vr}(T_v,T_r)}\,\frac{\sum_{v,v'} q_{vv'}e^{-E_v/T_v}\left(I_1+I_2\right)}{2\Gamma(1.5)\sum_{v,v'}\left(\frac{B_{e,v}}{300}\right)^{-3/2} q_{vv'}e^{-E_v/300}} \tag{A13}$$

B. Electron Impact Disscociation

The electron impact dissociation rates are given a similar treatment to excitation. In the case of dissociation, it is not necessary to sum over the upper state, and it is assumed there is an equal probability of dissociation for vibrational levels (i.e. no q_v factor). This yields the following equations:

$$\begin{aligned} k &= \frac{\sum_v S_v e^{-E_v/T_v}}{Q_{vr}} \\ S_v &= 5.47\times10^{-11}\sqrt{T_e(K)}I \\ I &= \int_0^{J_{\max}} 2J\exp\left[-\frac{D_e-E_v}{T_e}-\left(\frac{B_e}{T_r}-\frac{B_e}{T_e}\right)J^2\right]\left(C-B\frac{B_e}{T_e}J^2\right)dJ \\ C &= \frac{(D_e-E_v)}{T_e}B+A \end{aligned} \tag{B1}$$

where A and B are as defined in (A2). Correction of the cross-section to 300K is not required, as the summations in (A13) cancel when $q_{vv'} = 1.0$. It is noted here that an error was discovered in earlier versions of NEQAIR, where the dissociation energy of the molecule was substituted for the dissociation energy of the electronic state, D_e. This led to an underprediction of electron impact dissociation rate for excited molecular states in NEQAIR's non-Boltzmann solution.

The integral I has a solution given by:

$$I = \frac{1}{E}\mathrm{e}^{-\frac{D_e-E_v}{T_e}}\left[(C+BD)\left(1-\mathrm{e}^{-y_{\max}}\right)+BD\left(-y_{\max}\,\mathrm{e}^{-y_{\max}}\right)\right] \tag{B2}$$

where

$$\begin{aligned} D &= \frac{-B_e}{ET_e} \\ y_{\max} &= E\frac{D_e-E_v}{B_e} \\ E &= \frac{B_e}{T_r}-\frac{B_e}{T_e} \\ C &= \frac{D_e-E_v}{T_e}B+A \end{aligned} \tag{B3}$$

Substituting and reducing terms gives:

$$\begin{aligned} I &= \frac{T_{er}}{B_e}\mathrm{e}^{-\frac{D_e-E_v}{T_e}}\left[\left(A-B\frac{T_{er}}{T_e}\right)\left(1-\mathrm{e}^{-\frac{(D_e-E_v)}{T_{er}}}\right)+B\frac{D_e-E_v}{T_e}\right] \\ \frac{1}{T_{er}} &= \frac{1}{T_r}-\frac{1}{T_e} \end{aligned} \tag{B4}$$

There is a problem with this solution in that it appears to become unbounded if T_e=T_r, although the integral (B1) is not. Examining the limits would show that it is not unbounded, however machine accuracy will become an issue if it solved directly. A solution for small values of T_{er} is obtained by expanding the exponential. The expansion of (B4) yields:

$$I = \frac{D_e-E_v}{B_e}\mathrm{e}^{-\frac{D_e-E_v}{T_e}}\left\{A+B\frac{D_e-E_v}{2T_e}+\frac{(D_e-E_v)}{T_{er}}\left[\frac{A}{2}-\frac{B}{6}\frac{(D_e-E_v)}{T_e}\right]+O\left(T_{er}^{-2}\right)\right\} \tag{B5}$$

The first two terms above may be used to estimate the integral, and the third is used as an error metric. This expansion is applied when this error term is smaller than the machine error. Derivation of these errors is omitted from this Appendix, the result obtained suggests using the expansion when the following is satisfied:

$$\left|T_e - T_r\right| < T_e T_r \max\left[\eta_1^{-1/2}, \left(\frac{\varepsilon}{\eta_1\left(D_e - E_v\right)}\right)^{1/3}\right] \tag{B6}$$

where ε is the relative machine precision and

$$\eta_1 = \left(D_e - E_v\right)\left|\frac{AT_e}{2B} - \frac{D_e - E_v}{6}\right| \tag{B7}$$

Acknowledgments

The authors would like to thank NASA's MPCV Aerosciences Program and Entry Systems Modeling (ESM) project. Ramon Martinez, Mark McGlaughlin, James Joyce and David Bogdanoff are acknowledged for EAST testing. Brett Cruden and Aaron Brandis are supported through contract NNA15BB15C to AMA Inc.

References

1. Brandis, A. M., Johnston, C. O., Cruden, B. A., Prabhu, D., and Bose, D., "Uncertainty Analysis and Validation of Radiation Measurements for Earth Reentry," *Journal of Thermophysics and Heat Transfer,* Vol. 29, No. 2, 2015, pp. 209-221.
2. Cruden , B. A., "Absolute Radiation Measurements in Earth and Mars Entry Conditions," RTO-EN-AVT-218, 2014.
3. Wright, M. W., White, T., and Mangini, N., "Data Parallel Line Relaxation (DPLR) Code User Manual Acadia – Version 4.01.1," NASA/TM-2009-215388, October 2009.
4. Cruden , B. A., and Brandis, A. M., "Updates to the NEQAIR Radiation Solver," *Radiation in High Temperature Gases*. St. Andrews, UK, 2014.
5. Park, C., *Nonequilibrium Hypersonic Aerothermodynamics*, New York: John Wiley & Sons, 1990.
6. Park, C., "Review of chemical-kinetic problems of future NASA missions. I - Earth entries," *Journal of Thermophysics and Heat Transfer,* Vol. 7, No. 3, 1993, pp. 385-398.
7. Johnston, C. O., "Study of Aerothermodynamic Modeling Issues Relevant to High-Speed Sample Return Vehicles," VKI 2013-AVT-218.
8. Huo, W. M., Liu, Y., Panesi, M., Wray, A., and Carbon, D. F., "Electron-Impact Excitation Cross Sections for Modeling Non-Equilibrium Gas," AIAA Paper 2015-1896.
9. Gnoffo, P. A., Gupta, R. N., and Shinn, J. L., "Conservation Equations and Physical Models for Hypersonic Air Flows in Thermal and Chemical Nonequilibrium," NASA-TP-2867, Feb 1989.
10. Johnston, C. O., and Brandis, A. M., "Modeling of nonequilibrium CO Fourth-Positive and CN Violet emission in CO2–N2 gases," *Journal of Quantitative Spectroscopy and Radiative Transfer,* Vol. 149, 2014, pp. 303-317.
11. Fujita, K., Yamada, T., and Ishii, N., "Impact of Ablation Gas Kinetics on Hyperbolic Entry Radiative Heating," 2006.
12. Bose, D., and Candler, G. V., "Thermal rate constants of the O-2+ N-> NO+ O reaction based on the (2) A'and (4) A'potential-energy surfaces," *Journal of Chemical Physics,* Vol. 107, No. 16, 1997, pp. 6136-6145.
13. Bourdon, A., and Vervisch, P., "Study of a low-pressure nitrogen plasma boundary layer over a metallic plate," *Physics of Plasmas (1994-present),* Vol. 4, No. 11, 1997, pp. 4144-4157.
14. Teulet, P., Gonzalez, J., Mercado-Cabrera, A., Cressault, Y., and Gleizes, A., "One-dimensional hydro-kinetic modelling of the decaying arc in air–PA66–copper mixtures: I. Chemical kinetics, thermodynamics, transport and radiative properties," *Journal of Physics D: Applied Physics,* Vol. 42, No. 17, 2009, p. 175201.
15. Cruden, B. A., "Radiance Measurement for Low Density Mars Entry," AIAA Paper 2012-2742.
16. Brandis, A. M., Johnston, C. O., Cruden, B. A., and Prabhu, D. K., "Investigation of Nonequilibrium Radiation for Mars Entry," AIAA Paper 2013-1055.
17. Cruden, B. A., Martinez, R., Grinstead, J. H., and Olejniczak, J., "Simultaneous Vacuum Ultraviolet through Near IR Absolute Radiation Measurement with Spatiotemporal Resolution in an Electric Arc Shock Tube," AIAA Paper 2009-4240.
18. Bose, D., McCorkle, E., Bogdanoff, D., and Gary A. Allen, J., "Comparisons of Air Radiation Model with Shock Tube Measurements," AIAA 2009-1030.
19. McBride, B. J., and Gordon, S., "Computer program for calculation of complex chemical equilibrium compositions and applications II. User's Manual and Program Description," NASA RP-1311-P2, June 1996.
20. Koshi, M., Bando, S., Saito, M., and Asaba, T., "Dissociation of nitric oxide in shock waves," *Symposium (International) on Combustion,* Vol. 17, No. 1, 1979, pp. 553-562.

21. Tsang, W., and Herron, J. T., "Chemical Kinetic Data Base for Propellant Combustion I. Reactions Involving NO, NO2, HNO, HNO2, HCN and N2O," *Journal of Physical and Chemical Reference Data,* Vol. 20, No. 4, 1991, p. 609.
22. Thielen, K., and Roth, P., "Resonance absorption measurements of N and O atoms in high temperature no dissociation and formation kinetics," *Symposium (International) on Combustion,* Vol. 20, No. 1, 1985, pp. 685-693.
23. Cruden, B. A., Brandis, A. M., and Prabhu, D. K., "Compositional Dependence of Radiance in CO_2/N_2/Ar Systems," AIAA 2013-2502.
24. Baulch, D., Cobos, C., Cox, R., Frank, P., Hayman, G., Just, T., Kerr, J., Murrells, T., Pilling, M., and Troe, J., "Evaluated kinetic data for combustion modeling. Supplement I," *Journal of Physical and Chemical Reference Data,* Vol. 23, No. 6, 1994, pp. 847-848.
25. Bose, D., and Candler, G. V., "Thermal rate constants of the N2+O→NO+N reaction using ab initio 3A″ and 3A′ potential energy surfaces," *The Journal of Chemical Physics,* Vol. 104, No. 8, 1996, pp. 2825-2833.
26. Park, C., Jaffe, R. L., and Partridge, H., "Chemical-Kinetic Parameters of Hyperbolic Earth Entry," *Journal of Thermophysics and Heat Transfer,* Vol. 15, No. 1, 2001, pp. 76-90.
27. Levin, D. A., Braunstein, M., Candler, G. V., Collins, R. J., and Smith, G. P., "Examination of theory for bow shock ultraviolet rocket experiments. II," *Journal of Thermophysics and Heat Transfer,* Vol. 8, No. 3, 1994, pp. 453-459.
28. Cartry, G., Magne, L., and Cernogora, G., "Experimental study and modelling of a low-pressure N2–O2 time afterglow," *Journal of Physics D: Applied Physics,* Vol. 32, 1999, pp. 1894-1907.
29. Raiche, G. A., and Crosley, D. R., "Temperature dependent quenching of the A 2Σ+ and B 2Π states of NO," *The Journal of Chemical Physics,* Vol. 92, No. 9, 1990, pp. 5211-5217.
30. Thoman, J. W., Gray, J. A., Durant, J. L., and Paul, P. H., "Collisional electronic quenching of NO A 2Σ+ by N2 from 300 to 4500 K," *The Journal of Chemical Physics,* Vol. 97, No. 11, 1992, pp. 8156-8163.
31. Asscher, M., and Haas, Y., "The quenching mechanism of electronically excited Rydberg states of nitric oxide," *The Journal of Chemical Physics,* Vol. 76, No. 5, 1982, pp. 2115-2126.
32. Laux, C. O., "Optical diagnostics and radiative emission of air plasmas." Stanford University, 1993.
33. Park, C., and Menees, G. P., "Odd nitrogen production by meteoroids," *Journal of Geophysical Research: Oceans,* Vol. 83, No. C8, 1978, pp. 4029-4035.
34. Imami, M., and Borst, W. L., "Electron impact excitation of the gamma bands of nitric oxide," *The Journal of Chemical Physics,* Vol. 63, No. 8, 1975, pp. 3602-3605.
35. Krishnakumar, E., and Srivastava, S. K., "Cross sections for the dissociative attachment of electrons to NO," *J Phys B: At. Mol. Opt. Phys.,* Vol. 21, 1988, pp. L607-L609.
36. Capitelli, M., Ferreira, C. M., Gordiets, B. F., and Osipov, A. I., *Plasma Kinetics in Atmospheric Gases*, New York, NY: Springer-Verlag, 2000.
37. Dilecce, G., "Optical spectroscopy diagnostics of discharges at atmospheric pressure," *Plasma Sources Science and Technology,* Vol. 23, No. 1, 2014, p. 015011.
38. Bak, M. S., Kim, W., and Cappelli, M. A., "Quenching of Excited Electronic States of Molecular Nitrogen in Nanosecond Pulsed Discharges in Atmospheric Pressure Air," AIAA Paper 2011-1150.
39. Park, C., "Nonequilibrium Air Radiation (NEQAIR) Program: User's Manual," NASA TM 86707.
40. Itikawa, Y., "Cross sections for electron collisions with nitrogen molecules," *Journal of Physical and Chemical Reference Data,* Vol. 35, No. 1, 2006, pp. 31-53.
41. Sharma, S. P., Gillespie, W. D., and Meyer, S. A., "Shock front radiation measurements in air," *AIAA*. 1991, 91-0573.
42. Grover, M. S., Singh, N., Schwartzentruber, T. E., and Jaffe, R. L., "Dissociation and internal excitation of molecular nitrogen due to N2-N collisions using direct molecular simulation," 2017.
43. Jaffe, R. L., Schwenke, D. W., Grover, M., Valentini, P., Schwartzentruber, T. E., Venturi, S., and Panesi, M., "Comparison of quantum mechanical and empirical potential energy surfaces and computed rate coefficients for N2 dissociation," 2016.
44. Pierrot, L., Yu, L., Gessman, R., Laux, C., and Kruger, C., "Collisional-radiative modeling of nonequilibrium effects in nitrogen plasmas," 1999.
45. Heays, A. N., "Photoabsorption and Photodissociation in Molecular Nitrogen." Australian National University, 2010.
46. Crandall, D. H., Kauppila, W. E., Phaneuf, R. A., Taylor, P. O., and Dunn, G. H., "Absolute cross sections for electron-impact excitation ofN2+," *Physical Review A,* Vol. 9, No. 6, 1974, pp. 2545-2551.
47. Orel, A. E., Rescigno, T. N., and Lengsfield Iii, B. H., "Theoretical study of electron-impact excitation ofN2+," *Physical Review A,* Vol. 42, No. 9, 1990, pp. 5292-5297.
48. Tabata, T., Shirai, T., Sataka, M., and Kubo, H., "Analytic cross sections for electron impact collisions with nitrogen molecules," *Atomic Data and Nuclear Data Tables,* Vol. 92, No. 3, 2006, pp. 375-406.
49. Little, D. A., Chakrabarti, K., Mezei, J. Z., Schneider, I. F., and Tennyson, J., "Dissociative recombination ofN2+: An ab-initio study," *Physical Review A,* Vol. 90, No. 5, 2014.
50. Lemal, A., Jacobs, C. M., Perrin, M. Y., Laux, C. O., Tran, P., and Raynaud, E., "Prediction of Nonequilibrium Air Plasma Radiation Behind a Shock Wave," *Journal of Thermophysics and Heat Transfer*, 2015, pp. 1-14.
51. Tayal, S. S., and Zatsarinny, O., "B-spline R-matrix-with-pseudostates approach for excitation and ionization of atomic oxygen by electron collisions," *Physical Review A,* Vol. 94, No. 4, 2016.
52. Wang, Y., Zatsarinny, O., and Bartschat, K., "B-spline R-matrix-with-pseudostates calculations for electron-impact excitation and ionization of nitrogen," *Physical Review A,* Vol. 89, No. 6, 2014.

53. Lopez, B. E., Johnston, C. O., and Panesi, M., "Improved Non-Boltzmann Modeling for Nitrogen Atoms," 2016.
54. Peverall, R., Rosén, S., Peterson, J. R., Larsson, M., Al-Khalili, A., Vikor, L., Semaniak, J., Bobbenkamp, R., Le Padellec, A., Maurellis, A. N., and van der Zande, W. J., "Dissociative recombination and excitation of O2+: Cross sections, product yields and implications for studies of ionospheric airglows," *The Journal of Chemical Physics,* Vol. 114, No. 15, 2001, pp. 6679-6689.
55. Vejby-Christensen, L., Kella, D., Pedersen, H. B., and Andersen, L. H., "Dissociative recombination of NO 𝛆," *Physical Review A,* Vol. 57, No. 5, 1998, pp. 3627-3634.
56. Peterson, J. R., Le Padellec, A., Danared, H., Dunn, G. H., Larsson, M., Larson, A., Peverall, R., Strömholm, C., Rosén, S., af Ugglas, M., and van der Zande, W. J., "Dissociative recombination and excitation of N2+: Cross sections and product branching ratios," *The Journal of Chemical Physics,* Vol. 108, No. 5, 1998, pp. 1978-1988.
57. Florescumitchell, A., and Mitchell, J., "Dissociative recombination," *Physics reports,* Vol. 430, No. 5-6, 2006, pp. 277-374.
58. Phelps, A. V., "Cross Sections and Swarm Coefficients for Nitrogen Ions and Neutrals in N2 and Argon Ions and Neutrals in Ar for Energies from 0.1 eV to 10 keV," *J. Phys. Chem. Ref. Data,* Vol. 20, No. 3, 1990, pp. 557-573.
59. Higdon, K. J., Goldstein, D. B., and Varghese, P. L., "Sensitivity Analysis of DSMC Parameters for Ionizing Hypersonic Flows," 2015.
60. Moran, T. F., and Wilcox, J. B., "Charge transfer reactions of ground N+(3P) and excited N+(1D) state ions with neutral molecules," *The Journal of Chemical Physics,* Vol. 70, No. 3, 1979, pp. 1467-1473.
61. Bose, D., Wright, M. J., Bogdanoff, D. W., Raiche, G. A., and Allen Jr., G. A., "Modeling and Experimental Assessment of CN Radiation Behind a Strong Shock Wave," *Journal of Thermophysics and Heat Transfer,* Vol. 20, No. 2, 2006, pp. 220–230.
62. Pierrot, L., Laux, C., and Kruger, C., "Vibrationally-specific collisional-radiative model for nonequilibrium nitrogen plasmas," 1998.

Table 10. Constant (C) in the internal excitation rate for N

i / j	2	3	4	5	6	7	8	9	10	11	12	13	14	15	16	17	18	19	20	21	22
1	1.1E-08	3.5E-09	5.4E-10	1.0E-09	4.0E-09	1.0E-30	3.5E-10	1.5E-09	1.4E-09	5.9E-09	1.8E-10	1.6E-09	1.0E-30	1.0E-30	3.9E-11	1.0E-30	1.1E-11	1.9E-05	2.1E-05	2.2E-05	1.0E-30
2		5.4E-09	1.0E-30	2.8E-09	1.0E-30	6.8E-09	5.7E-10	2.0E-09	7.9E-10	3.3E-09	2.6E-10	1.8E-09	1.0E-30	1.0E-30	3.4E-10	1.0E-30	5.7E-06	6.3E-06	7.0E-06	7.6E-06	8.1E-06
3			1.0E-30	4.9E-09	1.0E-30	7.1E-09	9.4E-10	5.6E-09	3.9E-09	3.6E-09	7.3E-06	4.4E-09	1.0E-30	1.0E-30	8.4E-10	1.0E-30	4.5E-06	5.1E-06	5.6E-06	6.1E-06	6.6E-06
4				7.3E-12	9.2E-07	2.4E-08	6.6E-08	1.1E-07	3.5E-09	2.0E-08	1.8E-07	1.2E-07	4.2E-08	7.8E-08	1.7E-07	1.1E-07	2.1E-07	2.5E-07	2.9E-07	3.2E-07	3.6E-07
5					2.2E-07	5.6E-07	7.2E-08	8.0E-09	2.3E-07	1.9E-08	1.4E-07	1.4E-07	4.8E-08	1.1E-08	2.1E-07	1.3E-07	2.7E-07	3.3E-07	3.7E-07	4.2E-07	4.7E-07
6						2.2E-12	7.6E-07	1.3E-05	1.7E-05	1.4E-08	3.4E-07	4.8E-06	1.9E-08	1.3E-08	3.0E-07	3.4E-08	5.2E-07	7.2E-08	8.4E-08	9.7E-08	1.1E-07
7							1.1E-08	5.4E-05	2.3E-05	1.9E-08	1.2E-06	1.0E-05	1.4E-08	1.0E-07	1.3E-06	2.1E-08	1.0E-07	1.3E-07	1.5E-07	1.7E-07	2.0E-07
8								4.5E-11	4.4E-11	2.3E-05	1.8E-08	6.5E-08	1.8E-08	8.6E-06	1.5E-07	6.8E-08	4.5E-07	5.9E-07	7.2E-07	8.5E-07	9.8E-07
9									6.5E-18	6.0E-04	2.7E-09	1.8E-08	1.1E-07	1.3E-03	4.6E-08	1.4E-07	1.3E-07	1.7E-07	2.1E-07	2.5E-07	2.8E-07
10										1.4E-03	2.5E-09	1.6E-08	1.2E-07	2.9E-03	4.5E-08	1.6E-07	1.6E-07	2.1E-07	2.6E-07	3.1E-07	3.6E-07
11											2.7E-04	7.0E-03	1.8E-08	5.0E-08	4.1E-04	4.5E-08	3.3E-04	2.8E-07	3.5E-07	4.2E-07	4.9E-07
12												5.4E-12	5.4E-11	1.8E-07	9.8E-08	4.9E-08	1.3E-08	9.1E-09	8.5E-09	8.6E-09	9.2E-09
13													1.1E-13	5.2E-10	2.5E-08	1.2E-07	2.1E-07	2.9E-07	3.8E-07	4.6E-07	5.5E-07
14														2.1E-10	4.7E-09	3.4E-08	3.2E-08	4.5E-08	5.9E-08	7.3E-08	8.7E-08
15															7.1E-09	3.0E-08	2.9E+02	7.8E-09	8.4E-09	9.1E-09	1.0E-08
16																1.2E-13	1.6E-08	3.2E-08	4.7E-08	6.0E-08	7.3E-08
17																	2.7E-09	5.8E-09	8.5E-09	1.1E-08	1.4E-08
18																		3.1E-08	5.3E-05	7.2E-05	8.2E-05
19																			3.2E-08	5.6E-08	7.7E-08
20																				3.3E-08	6.0E-08
21																					3.4E-08

Table 11. Exponent (n) in the internal excitation rate for N

i / j	2	3	4	5	6	7	8	9	10	11	12	13	14	15	16	17	18	19	20	21	22
1	0.20	0.21	0.26	-0.12	0.82	0.00	-0.13	-0.21	-0.22	0.82	-0.11	-0.19	0.00	0.00	0.30	0.00	0.17	-2.09	-2.09	-2.09	0.00
2		0.27	0.00	-0.10	0.00	0.62	-0.22	-0.24	-0.04	0.79	-0.28	-0.22	0.00	0.00	0.26	0.00	-2.07	-2.07	-2.07	-2.07	-2.07
3			0.00	-0.10	0.00	0.59	-0.33	-0.25	-0.14	0.76	-1.88	-0.20	0.00	0.00	0.00	0.00	-2.06	-2.07	-2.07	-2.07	-2.07
4				-0.43	-0.15	-0.38	-0.12	-0.16	-0.72	-0.41	-0.11	-0.22	-0.23	-0.30	-0.26	-0.28	-0.32	-0.33	-0.33	-0.33	-0.33
5					-0.21	-0.18	-0.14	-0.71	-0.18	-0.43	-0.10	-0.25	-0.28	-0.45	-0.27	-0.32	-0.35	-0.35	-0.36	-0.36	-0.36
6						-1.09	-0.35	-0.45	-0.50	-0.17	-0.61	-0.51	-0.44	-0.27	-0.49	-0.43	-0.65	-0.33	-0.34	-0.35	-0.35
7							0.16	-0.48	-0.45	-0.25	-0.62	-0.51	-0.52	-0.25	-0.49	-0.46	-0.37	-0.39	-0.40	-0.40	-0.41
8								-0.44	-0.49	-0.39	-0.05	0.07	0.13	-0.57	-0.05	-0.01	-0.37	-0.43	-0.46	-0.48	-0.49
9									-0.96	-0.39	0.07	-0.10	0.08	-0.49	-0.20	0.04	-0.20	-0.27	-0.31	-0.33	-0.35
10										-0.39	-0.39	-0.07	0.04	-0.49	-0.19	0.00	-0.27	-0.34	-0.38	-0.40	-0.42
11											-0.67	-0.69	-0.37	-0.17	-0.68	-0.46	-0.82	-0.52	-0.59	-0.63	-0.65
12												-0.51	-0.49	0.22	0.33	0.30	0.26	-0.05	-0.22	-0.38	-0.49
13													-0.33	-0.15	0.31	0.30	-0.63	-0.82	-0.97	-1.05	-1.11
14														-0.50	-0.38	0.28	-0.49	-0.70	-0.84	-0.94	-1.00
15															0.45	-0.31	-1.05	-0.15	-0.32	-0.47	-0.58
16																-0.38	-0.05	-0.37	-0.54	-0.69	-0.80
17																	0.08	-0.23	-0.40	-0.56	-0.67
18																		0.18	-0.16	-0.31	-0.45
19																			0.24	-0.12	-0.25
20																				0.28	-0.10
21																					0.30

Table 12. Constant (C) in the internal excitation rate for O

i / j	2	3	4	5	6	7	8	9	10	11	12	13	14	15	16	17	18	19
1	2.3E-09	3.8E-10	8.8E-15	1.9E-09	5.7E-09	3.4E-09	1.1E-10	2.4E-10	2.7E-08	2.7E-11	1.1E-10	1.0E-30	4.1E-11	3.4E-11	1.7E-11	1.0E-11	5.5E-12	3.7E-12
2		1.3E-09	3.2E-17	1.9E-14	1.0E-30	1.0E-30	9.6E-16	9.0E-15	1.0E-30	1.0E-30	1.0E-30	1.0E-30	1.0E-30	0.0E+00	0.0E+00	0.0E+00	0.0E+00	0.0E+00
3			1.0E-30	7.9E-17	1.0E-30	1.0E-30	1.0E-17	6.0E-14	1.0E-30	1.0E-30	1.0E-30	1.0E-30	1.0E-30	0.0E+00	0.0E+00	0.0E+00	0.0E+00	0.0E+00
4				1.0E-30	6.7E-07	4.7E-12	1.0E-30	1.0E-30	4.6E-10	1.0E-30	1.0E-30	5.2E-12	1.0E-30	9.9E-15	2.6E-13	2.9E-13	2.4E-13	1.9E-13
5					2.2E-11	1.3E-06	1.0E-30	1.0E-30	1.5E-09	1.0E-30	1.0E-30	7.7E-11	1.0E-30	6.9E-12	4.5E-13	3.2E-15	2.8E-14	6.2E-14
6						4.6E-12	2.2E-07	7.3E-07	2.5E-09	5.2E-09	1.8E-08	1.6E-08	2.9E-09	2.2E-09	7.5E-10	3.4E-10	1.6E-10	9.2E-11
7							3.6E-07	1.6E-06	7.9E-08	1.0E-08	2.3E-08	8.6E-08	2.5E-09	3.3E-09	1.0E-09	4.2E-10	1.8E-10	1.1E-10
8								1.0E-30	8.8E-06	1.0E-30	1.0E-30	2.4E-08	1.0E-30	1.8E-09	2.6E-10	6.6E-11	2.3E-11	9.8E-12
9									2.2E-06	1.0E-30	1.9E-06	3.1E-09	1.3E-07	2.9E-08	1.1E-08	4.1E-09	2.2E-09	1.3E-09
10										2.3E-06	6.3E-06	8.2E-09	1.9E-07	1.1E-07	2.2E-08	7.9E-09	3.1E-09	1.7E-09
11											1.0E-30	4.0E-05	1.0E-30	1.6E-07	1.1E-08	2.2E-09	6.8E-10	2.7E-10
12												5.3E-06	2.3E-06	2.1E-07	5.4E-08	1.7E-08	8.0E-09	4.4E-09
13													2.1E-05	1.4E-05	4.1E-07	8.9E-08	2.8E-08	1.3E-08
14														2.5E-05	5.6E-07	1.2E-07	4.6E-08	2.2E-08
15															3.8E-05	8.9E-07	2.2E-07	8.4E-08
16																1.2E-05	1.7E-06	4.3E-07
17																	4.4E-05	3.0E-06
18																		6.2E-05

Table 13. Exponent (n) in the internal excitation rate for O

i / j	2	3	4	5	6	7	8	9	10	11	12	13	14	15	16	17	18	19
1	0.47	0.24	0.04	0.04	0.07	0.81	0.22	0.13	0.17	0.19	0.16	0.00	0.17	0.03	0.11	0.16	0.26	0.27
2		-0.03	0.01	0.02	0.00	0.00	0.18	0.09	0.00	0.00	0.00	0.00	0.00	0.00	0.00	0.00	0.00	0.00
3			0.00	-0.01	0.00	0.00	0.16	0.06	0.00	0.00	0.00	0.00	0.00	0.00	0.00	0.00	0.00	0.00
4				0.00	-0.07	-0.05	0.00	0.00	0.00	0.00	0.00	0.07	0.00	-0.03	0.15	0.22	0.27	0.30
5					-0.09	-0.07	0.00	0.00	0.13	0.00	0.00	0.12	0.00	0.00	0.16	0.23	0.28	0.31
6						-1.19	-0.15	-0.06	-0.19	0.01	0.05	-0.05	0.11	-0.12	0.03	0.13	0.27	0.31
7							0.01	-0.06	-0.54	0.07	0.04	-0.26	0.10	-0.18	-0.02	0.08	0.23	0.28
8								0.00	-0.13	0.00	0.00	-0.04	0.00	-0.12	0.07	0.15	0.22	0.26
9									-0.22	0.00	-0.06	-0.07	0.02	0.09	0.11	0.24	0.27	0.30
10										-0.14	-0.13	-0.15	-0.03	-0.29	-0.09	0.02	0.18	0.23
11											0.00	-0.23	0.00	-0.27	-0.06	0.04	0.11	0.16
12												-0.29	-0.14	-0.05	-0.01	0.12	0.16	0.20
13													-0.15	-0.50	-0.21	-0.07	0.11	0.17
14														-0.41	-0.12	0.03	0.08	0.11
15															-0.25	-0.04	0.06	0.11
16																-0.11	-0.06	0.00
17																	-0.24	-0.12
18																		-0.27